REPORT DOCUMENTATION PAGE

Form Approved OMB NO. 0704-0188

1. REPORT DATE (DD-MM-YYYY)	2. REPORT TYPE	3. DATES COVERED (From - To)
26-09-2017	Final Report	10-Sep-2012 - 31-Mar-2017

4. TITLE AND SUBTITLE
Final Report: Dynamic Failure Mitigation Through Microstructure Control: Application to Aluminum and Magnesium Alloys

5a. CONTRACT NUMBER
W911NF-12-1-0455

5b. GRANT NUMBER

5c. PROGRAM ELEMENT NUMBER
611102

6. AUTHORS

5d. PROJECT NUMBER

5e. TASK NUMBER

5f. WORK UNIT NUMBER

7. PERFORMING ORGANIZATION NAMES AND ADDRESSES
University of Virginia
1001 North Emmet Street
P. O. Box 400195
Charlottesville, VA 22904 -4195

8. PERFORMING ORGANIZATION REPORT NUMBER

9. SPONSORING/MONITORING AGENCY NAME(S) AND ADDRESS (ES)
U.S. Army Research Office
P.O. Box 12211
Research Triangle Park, NC 27709-2211

10. SPONSOR/MONITOR'S ACRONYM(S)
ARO

11. SPONSOR/MONITOR'S REPORT NUMBER(S)
61406-MS.12

12. DISTRIBUTION AVAILIBILITY STATEMENT
Approved for public release; distribution is unlimited.

13. SUPPLEMENTARY NOTES
The views, opinions and/or findings contained in this report are those of the author(s) and should not contrued as an official Department of the Army position, policy or decision, unless so designated by other documentation.

14. ABSTRACT

15. SUBJECT TERMS

16. SECURITY CLASSIFICATION OF:			17. LIMITATION OF ABSTRACT	15. NUMBER OF PAGES	19a. NAME OF RESPONSIBLE PERSON
a. REPORT	b. ABSTRACT	c. THIS PAGE			Sean Agnew
UU	UU	UU	UU		19b. TELEPHONE NUMBER 434-924-0605

RPPR Final Report
as of 27-Sep-2017

Agency Code:

Proposal Number: 61406MS **Agreement Number: W911NF-12-1-0455**
INVESTIGATOR(S):

Name: Sean R. Agnew
Email: agnew@virginia.edu
Phone Number: 4349240605
Principal: Y

Name: Haitham El Kadiri
Email: elkadiri@me.msstate.edu
Phone Number: 6623254777
Principal: N

Organization: **University of Virginia**
Address: 1001 North Emmet Street, Charlottesville, VA 229044195
Country: USA
DUNS Number: 065391526 EIN: 546001796

Report Date: 30-Jun-2017 Date Received: 26-Sep-2017
Final Report for Period Beginning 10-Sep-2012 and Ending 31-Mar-2017
Title: Dynamic Failure Mitigation Through Microstructure Control: Application to Aluminum and Magnesium Alloys
Begin Performance Period: 10-Sep-2012 **End Performance Period:** 31-Mar-2017
Report Term: 0-Other

Submitted By: Sean Agnew Email: agnew@virginia.edu
Phone: (434) 924-0605

STEM Degrees: 1 **STEM Participants:** 5

Major Goals: The overall goal of the project was to determine the microstructure design principles necessary to optimize the mechanical behavior of precipitation strengthened Al and Mg alloys. We have selected three alloys (AA6055, AA7085, and Mg alloy, WE43) together with industrial partners, ALCOA (now Arconic) and Magnesium Elektron N.A., who have provided the material in their optimized tempers for armor applications. We also heat treated alloys AA7085 and WE43 to examine them in solution heat treated (T3), under-aged, and peak-aged (T6) conditions. WE43 was also examined in the solution heat treated, stretched, and peak-aged (T8) condition. Previous interim reports emphasized constitutive data obtained at quasi-static and dynamic strain rates, as well as microstructure data, including electron backscattered diffraction (EBSD) data obtained from as-received and deformed samples. This final report summarizes our major findings and achievements, with an emphasis on the past two years of the project.

Accomplishments: In the past two years, we have made five noteworthy achievements described briefly below, which are also described with graphics in the attached 2 power point slides. All the published references are provided in the 'Dissemination' section. The papers that are in review are attached.

1. We have demonstrated that a new high strength Al alloy (AA7085 in T711 and T721 tempers) that has recently been contemplated as a candidate lightweight metallic armor plate material by the Army exhibits a lower level of plastic anisotropy at quasi-static and dynamic strain rates than one would expect, given the significant crystallographic texture observed in the plate material. This is good news for design engineers, since a highly anisotropic response would greatly complicate the design process. This result has been presented at international conferences and a paper is published in International Journal of Plasticity (see ref. [4] in 'Dissemination'). Additional testing of the material, in solution heat treated and quenched as well as peak aged conditions, shows that this tendency toward isotropy is clearly connected with the presence of precipitates (see appended paper [1] in review with International Journal of Plasticity).
2. We have implemented a multi-scale, elastoplastic self-consistent (EPSC) polycrystalline deformation model, which predicts the observed behavior. The results of the modeling validate the hypothesis that precipitates can alter the anisotropy of an age-hardenable alloy, with a trend toward isotropy. The essential concept is that “backstresses” enforced by the precipitates on the surrounding alloy matrix cause alternative slip systems to be activated, rather than continuing to deform on the initially activated slip systems which would lead to anisotropy.

Note that neither grain shape effects nor traditional latent hardening approaches can reproduce the experimentally observed phenomenon. This work represents the first demonstration of the impact that multi-scale, precipitate-grain-polycrystal interactions can have on plastic anisotropy. See attached presentation slide for illustrations and summary of the formulation. See also appended paper [1] in review with International Journal of Plasticity.
3. A study of various aging protocols to strengthen Mg alloy WE43 shows that the commercially processed condition (T5 - hot-rolled and aged) is the optimum condition as regards strength, ductility, and processing cost (since no solutionizing heat treatment required). Other strategies (T6 - solutionize plus artificial age or T8 – solutionize, stretch, plus artificial age) can achieve equal hardness. However, the ductility is lowered due to creation of precipitate free zones (PFZs). The details of this study are provided in paper [3].
4. Transmission electron microscopy of WE43 in the T5 and T6 tempers reveals that the strengthening precipitates are shearable. This has profound implications for alloy designers, since the prismatic plate shaped precipitates are rendered as less effective strengtheners than previously supposed. New integrated computational materials engineering (ICME) strategies will have to consider precipitate shearability. See appended paper [2] in review with Acta Materialia.
5. A multi-scale, elastoplastic self-consistent (EPSC) polycrystalline deformation model has been developed to predicts the strength of Mg alloys, given the texture, grain size, solid solution alloy content, precipitate microstructure (shape, size, & volume fraction) & shearability of those precipitates (in terms of anti-phase domain boundary (APB) energy). The model was trained using data from T5 material and then used to predict the behavior of T6 (with very different crystallographic texture and grain size). The details of these last two achievements are documented in papers [2] and [6] and summarized in the presentation slides.

Training Opportunities: 5 students worked in support of the project.
1. Jishnu Bhattacharyya performed most of his doctoral research under the purview of this project. He learned texture analysis, high strain rate testing, and crystal plasticity modeling.

2. Fulin Wang supported this project by performing TEM on Mg alloy, WE43, and analytical modeling of precipitation strengthening. He was co-sponsored by an NSF program.

3. Mechanical Engineering B.S. student, Bradley Bittmann, was trained to perform quasi-static and high strain rate tests along with microstructure characterization using SEM and EBSD. His testing and analysis served as the basis for one of the papers prepared during the project, earning him co-authorship of the paper, reference number [1] in the dissemination section of this report.

4. Materials Science and Engineering B.S. student (of Cornell University), Meredith Lee, was trained to perform microstructure characterization using SEM and EBSD. Her microstructure analysis was employed in one of the papers prepared during the project, earning her co-authorship of the paper, reference number [4] in the dissemination section of this report. Her summer internship was co-sponsored by industry.

5. Chemical Engineering B.S. student, Patrick McQuade, was trained to perform heat treatment, hardness measurement, tensile testing, and microstructure characterization. His experimental data was employed in one of the papers prepared during the project, earning him co-authorship of the paper, reference number [3] in the dissemination section of this report. His summer and senior year research internship was co-sponsored by the Virginia Space Grant Consortium.

RPPR Final Report
as of 27-Sep-2017

Results Dissemination: 1. Bhattacharyya, J.J., Bittmann, B., Agnew, S.R. (2017). Effect of precipitates on anisotropy - Application to aluminum alloy, 7085. International Journal of Plasticity in review.
2. Bhattacharyya, J.J., Wang, F., Stanford, N., Agnew, S.R. (2017). Slip mode dependency of dislocation shearing and looping of precipitates in Mg alloy WE43 Shearable WE43. Acta Materialia, in review.
3. Bhattacharyya, J.J., Wang, F., McQuade, P.J., Agnew, S.R. (2017). Deformation and fracture behavior of Mg alloy, WE43, after various aging heat treatments. Materials Science and Engineering A, 705, 79-88.
4. Bhattacharyya, J. J., Agnew, S. R., Lee, M. M., Whittington, W. R., & El Kadiri, H. (2017). Measuring and modeling the anisotropic, high strain rate deformation of Al alloy, 7085, plate in T711 temper. International Journal of Plasticity, 93, 46-63.
5. Agnew, S. R., Bhattacharyya, J. J., Wang, F., & McQuade, P. J. (2017). Using the Crystal Plasticity Approach to Parse the Effects of Alloying and Aging on the Mechanical Behavior of Wrought Mg Alloys. Magnesium Technology 2017, pp. 13-15. Springer International Publishing.
6. Bhattacharyya, J. J., Wang, F., Wu, P. D., Whittington, W. R., El Kadiri, H., & Agnew, S. R. (2016). Demonstration of alloying, thermal activation, and latent hardening effects on quasi-static and dynamic polycrystal plasticity of Mg alloy, WE43-T5, plate. International Journal of Plasticity, 81, 123-151.
7. Wang, F., Bhattacharyya, J. J., & Agnew, S. R. (2016). Effect of precipitate shape and orientation on Orowan strengthening of non-basal slip modes in hexagonal crystals, application to magnesium alloys. Materials Science and Engineering: A, 666, 114-122.
8. Agnew, S. R., Calhoun, C. A., & Bhattacharyya, J. J. (2016). What is in a Strain Hardening “Plateau”? Magnesium Technology 2016, pp. 189-194. Springer International Publishing.
9. J. Bhattacharyya, S. Agnew, P. Wu, W. Wittington, and H. El Kadiri. (2015) Crystal Plasticity Modeling of the Dynamic Behavior of Magnesium Alloy, WE43?T5, Plate. Magnesium Technology 2015, pp. 165-170. Springer International Publishing.
10. Qiao, H., Agnew, S. R., & Wu, P. D. (2015). Modeling twinning and detwinning behavior of Mg alloy ZK60A during monotonic and cyclic loading. International Journal of Plasticity, 65, 61-84.
11. Agnew, S., Wu, P., Inal, K., El Kadiri, H., Wang, J., & Tome, C. (2015). Measuring and Modeling the Effects of Mechanical Twinning on the Behavior of Magnesium Alloys. In Magnesium Technology 2015, pp. 15-17. Springer International Publishing.
12. Agnew, S.R., Whittington, W.R., Oppedal, A., El Kadiri, H., Shaeffer, M., Ramesh, K.T. Bhattacharyya, J.J., Delorme, R., Davis. B. (2014). "Dynamic behavior of a rare-earth-containing Mg alloy, WE43B-T5, plate with comparison to conventional alloy, AM30-F." JOM 66(2), 277-290.
13. Agnew, S. R., Calhoun, C. A., & Clausen, B. (2014). In-situ Neutron diffraction study of aging in alloy ZK60A. In Magnesium Technology 2014 (pp. 389-394). Springer International Publishing.

Honors and Awards: 1. Plenary lecture delivered at the Magnesium Technology 2017 Symposium, held within the TMS 2017 Annual Meeting in San Diego, CA, February, 2017. Jishnu Bhattacharyya, Fulin Wang, & Sean Agnew, “A comprehensive strengthening model for Mg alloys: Describing the aging response of alloy WE43 --- Toward Integrated Computational Materials Engineering (ICME) of wrought magnesium alloys.”
2. Invited lecture at the International Symposium on Plasticity and Damage, Puerto Vallarta, Mexico, January 2017. Jishnu Bhattacharyya, Fulin Wang, & Sean Agnew, “A comprehensive strengthening model for Mg alloys: Describing the aging response of alloy WE43.”
3. Invited lecture at the International Symposium on Plasticity and Damage, Puerto Vallarta, Mexico, January 2017. Jishnu Bhattacharyya & Sean Agnew, “Precipitation-induced anisotropy in aluminum alloy 7085 under quasistatic and dynamic loading.”
4. Invited lecture at the International Symposium on Plasticity and Damage, Kailua Kona, HI, January 2016. Jishnu Bhattacharyya, Sean Agnew, Meredith Lee, Wilburn Whittington, Haitham El Kadiri, “Measuring and modeling the anisotropic, high strain rate deformation of Al alloy, 7085, plate in T711 temper.”
5. Invited lecture at Magnesium Alloys and Their Applications Conference, Jeju, Korea, October 2015. S.R. Agnew, J.J. Bhattacharyya, C.A. Calhoun, K. Inal, E. Popova, A.P. Brahme, R.K. Mishra, “Measuring & modeling the effects of {10.2} twinning in Mg alloy ZK60A Twinning.”
6. Student paper of the year award, Magnesium Technology 2015 - for paper [6] in the list below, and the associated lecture. J. Bhattacharyya, S. Agnew, P. Wu, W. Wittington, and H. El Kadiri, “Crystal Plasticity Modeling of the Dynamic Behavior of Magnesium Alloy, WE43?T5, Plate.” Magnesium Technology 2015, (TMS-AIME: Warrendale, PA: 2015) pp. 165-170.
7. Invited lecture delivered at the Magnesium Technology 2014 Symposium. Agnew, S.R., Whittington, W.R., Oppedal, A., El Kadiri, H., Shaeffer, M., Ramesh, K.T. Bhattacharyya, J.J., Delorme, R., Davis. B. (2014). "Dynamic behavior of a rare-earth-containing Mg alloy, WE43B-T5, plate with comparison to conventional alloy, AM30-F."

RPPR Final Report
as of 27-Sep-2017

Protocol Activity Status:

Technology Transfer: ARL researchers formerly performed ballistics testing on alloys WE43-T5 & AA7085-T7XX. The results developed in the current program will support decisions made with respect to application of these lightweight alloys.

ARL researchers recently performed ballistics testing of AA6055-T6, which we also examined in the current program. We do not know if our previously reported results showing the dynamic response of this alloy played any role in their decision to perform this ballistics testing.

We collaborated with Mississippi State University (MSU) Profs. Haitham El Kadiri and Wilburn Whittington on another ARL-sponsored program, in which we are interacting closely with ARL researcher, Dr. Mark Tschopp, during the later stages of the presetn project. Together with Mark Tschopp, the PI helped researchers at MSU draft a paper about the static and dynamic recrystallization behavior of another Mg-rare earth element containing alloy (distinct from the alloy WE43 examined in this present project). This work is important because it is establishing the mechanisms by which rare earth elements impart texture alteration to wrought Mg alloys. Conventional wrought Mg alloys suffer from strong deformation textures, whereas those that contain rare earth elements can be processed to have weak or very distinct textures, which frequently impart much higher formability.

PARTICIPANTS:

Participant Type: PD/PI
Participant: Sean R Agnew
Person Months Worked: 4.00 **Funding Support:**
Project Contribution:
International Collaboration:
International Travel:
National Academy Member: N
Other Collaborators:

Participant Type: Faculty
Participant: Haitham El Kadiri
Person Months Worked: 1.00 **Funding Support:**
Project Contribution:
International Collaboration:
International Travel:
National Academy Member: N
Other Collaborators:

ARTICLES:

RPPR Final Report
as of 27-Sep-2017

Publication Type: Journal Article Peer Reviewed: Y **Publication Status:** 1-Published
Journal: JOM
Publication Identifier Type: DOI Publication Identifier: 10.1007/s11837-013-0830-x
Volume: 66 Issue: 2 First Page #: 277
Date Submitted: Date Published:
Publication Location:
Article Title: Dynamic Behavior of a Rare-Earth-Containing Mg Alloy, WE43B-T5, Plate with Comparison to Conventional Alloy, AM30-F
Authors:
Keywords: magnesium, aluminum, aging, texture, preferred orientation, anisotropy, asymmetry, high strain rate, split Hopkinson pressure bar, Kolsky bar
Abstract: The dynamic behavior of Mg alloys is an area of interest for applications, such as crash-sensitive automotive components and armor. The rare earth element-containing alloy, WE43B-T5, has performed well in ballistic testing, so the quasi-static (~10-3 1/s) and dynamic (~600 - 5000 1/s) mechanical behaviors of two Mg alloys, rolled WE43B-T5 and extruded AM30-F were investigated using servohydraulic and Kolsky bar testing in uniaxial tension and compression. The yield stress was surprisingly isotropic for WE43B-T5 relative to conventional Mg alloys (including extruded AM30-F). The WE43B plate was textured; however it was not the typical basal texture of hot-rolled Mg-Al alloys. The effect of strain rate on the yield strength of WE43B-T5 is small and the strain hardening behavior is only mildly rate sensitive (m = 0.008). The combination of high strength (~300 MPa), moderate ductility (0.07 – 0.20) and low density yield a material with good specific energy absorption capacity.
Distribution Statement: 1-Approved for public release; distribution is unlimited.
Acknowledged Federal Support:

Publication Type: Journal Article Peer Reviewed: Y **Publication Status:** 1-Published
Journal: Materials Science and Engineering: A
Publication Identifier Type: DOI Publication Identifier: 10.1016/j.msea.2016.04.056
Volume: 666 Issue: First Page #: 114
Date Submitted: 9/26/17 12:00AM Date Published: 6/1/16 4:00AM
Publication Location:
Article Title: Effect of precipitate shape and orientation on Orowan strengthening of non-basal slip modes in hexagonal crystals, application to magnesium alloys
Authors: Fulin Wang, Jishnu J. Bhattacharyya, Sean R. Agnew
Keywords: Magnesium alloys; Precipitate; Orowan strengthening; Non-basal slip
Abstract: Orowan equations predicting the strengthening of non-basal slip systems in hexagonal crystals are derived for rationally distributed, shear resistant precipitates of typical morphologies and orientations. These equations may be employed for any hexagonal crystal, but application is made specifically to hexagonal close packed Mg, where alloy development is presently quite active. Particular focus is placed on discerning the effect on ?c+a??c+a? dislocations, and generally speaking, ?c+a??c+a? slip is most potently strengthened by prismatic plate shaped precipitates, as was shown previously for basal and prismatic slip. If strengthening is the primary goal, prismatic plate shaped precipitates appear ideal. Because the motion of ?c+a??c+a? dislocations has been repeatedly emphasized as crucial for preserving ductility, it may be of interest to consider
Distribution Statement: 2-Distribution Limited to U.S. Government agencies only; report contains proprietary info
Acknowledged Federal Support: **Y**

CONFERENCE PAPERS:

Publication Type: Conference Paper or Presentation **Publication Status:** 1-Published
Conference Name: 2014 TMS Annual Meeting, Magnesium Technology 2014 Symposium
Date Received: 26-Sep-2017 Conference Date: 16-Feb-2014 Date Published:
Conference Location: San Diego Convention Center, San Diego, California
Paper Title: In-situ neutron diffraction study of aging in alloy ZK60A
Authors: Sean R. Agnew Christopher A. Calhoun Bjørn Clausen
Acknowledged Federal Support: **Y**

RPPR Final Report
as of 27-Sep-2017

Publication Type: Conference Paper or Presentation **Publication Status:** 1-Published
Conference Name: Magnesium Technology 2015
Date Received: 26-Sep-2017 Conference Date: 15-Mar-2015 Date Published:
Conference Location: Orlando Florida USA
Paper Title: Crystal plasticity modeling of the dynamic behavior of magnesium alloy, WE43-T5, plate
Authors: J. Bhattacharyya, S. Agnew, P. Wu, W. Wittington, and H. El Kadiri.
Acknowledged Federal Support: **Y**

Publication Type: Conference Paper or Presentation **Publication Status:** 1-Published
Conference Name: Magnesium Technology 2015
Date Received: 26-Sep-2017 Conference Date: 17-Mar-2015 Date Published: 17-Mar-2015
Conference Location: Orlando Florida USA
Paper Title: Measuring and Modeling the Effects of Mechanical Twinning on the Behavior of Magnesium Alloys
Authors: Agnew, S., Wu, P., Inal, K., El Kadiri, H., Wang, J., & Tome, C.
Acknowledged Federal Support: **Y**

Publication Type: Conference Paper or Presentation **Publication Status:** 1-Published
Conference Name: TMS Magnesium Technology 2016
Date Received: 26-Sep-2017 Conference Date: 15-Feb-2016 Date Published: 15-Feb-2016
Conference Location: Nashville Tennessee USA
Paper Title: WHAT IS IN A STRAIN HARDENING “PLATEAU”?
Authors: Sean R. Agnew, Christopher A. Calhoun, and Jishnu J. Bhattacharyya
Acknowledged Federal Support: **Y**

DISSERTATIONS:

Publication Type: Thesis or Dissertation
Institution: Univeristy of Virginia
Date Received: 26-Sep-2017 Completion Date: 8/10/16 7:45PM
Title: Quasi-static and dynamic constitutive behavior of precipitate strengthened Al and Mg alloys: An experimental and crystal plasticity modeling investigation
Authors: Bhattacharyya, Jishnu Jyoti
Acknowledged Federal Support: **N**

High strength AA7085-T7XX exhibits near isotropy, despite strong texture, rendering design implementation simpler. *Multi-scale crystal plasticity modeling provides explanation.*

Observation: Aging reduces plastic anisotropy, r-values tend toward 1

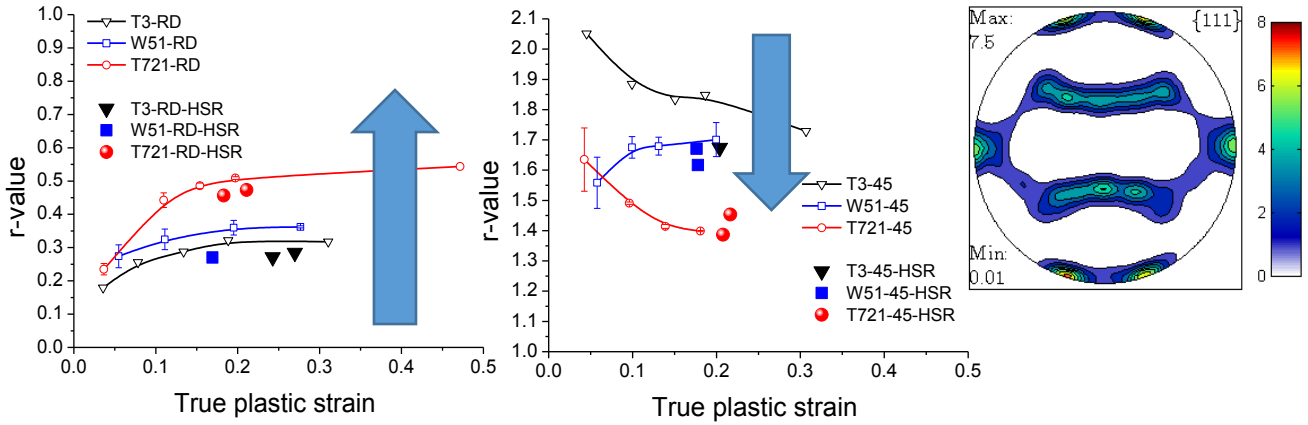

Hypothesis: Precipitates enforce backstress on grains alters slip system selection

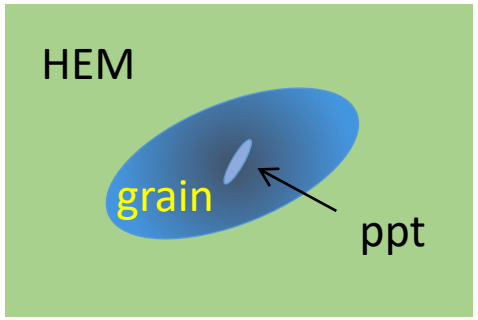

Multi-scale micromechanics: elastic inclusion in elastoplastic grain in polycrystal

$$d\varepsilon_{ij}^{c} = f d\varepsilon_{ij}^{ppt} + (1-f) d\varepsilon_{ij}^{m}$$
$$= f d\varepsilon_{ij}^{ppt} + (1-f) d\varepsilon_{ij}^{m,el} + d\varepsilon_{ij}^{m,pl}$$

$$d\sigma_{ij}^{c} = f d\sigma_{ij}^{ppt} + (1-f) d\sigma_{ij}^{m}$$

Model implementation: Backstress alters grain-level yield criterion

$$\tau_{CRSS,c}^{\alpha} = m_{ij}^{\alpha}\left(\sigma_{ij}^{c} - f\sigma_{ij}^{ppt}\right) = (1-f)\tau_{CRSS,m}^{\alpha}$$

Backstress depends on precipitate stiffness, strain concentration tensor, and the grain stress-state and elastoplastic stiffness

$$d\sigma_{ij}^{ppt} = C_{ijuv}^{ppt} T_{uvmn}^{ppt} (L_{mnkl}^{c})^{-1} d\sigma_{kl}^{c}$$

Backstress saturates with straining due to thermally activated relaxation mechanisms

$$T_{ijkl}^{ppt} = \left(C_{ijop}^{ppt} + L_{ijop}^{*}\right)^{-1} \left(L_{opkl}^{c} + L_{opkl}^{*}\right) \exp\left(-\frac{\varepsilon_{VM}^{c,p}}{\varepsilon_{sat}}\right)$$

Validation: Simulations predict correct trends in anisotropy development

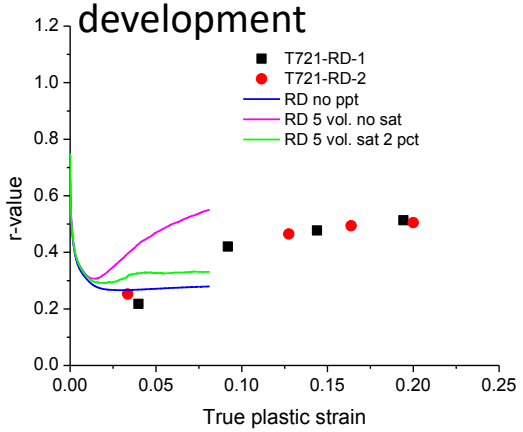

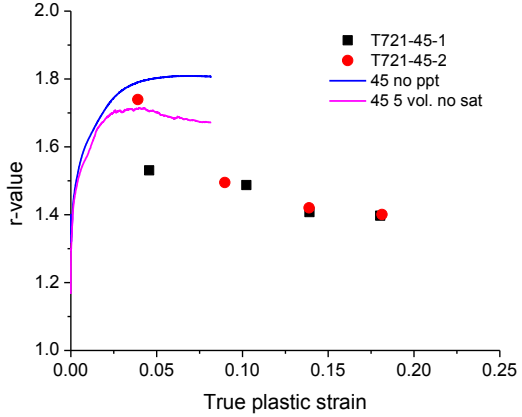

Strength modeling of Mg alloy WE43 requires consideration of shearable precipitates, and ductility is affected by grain boundary precipitates and associated precipitate free zones

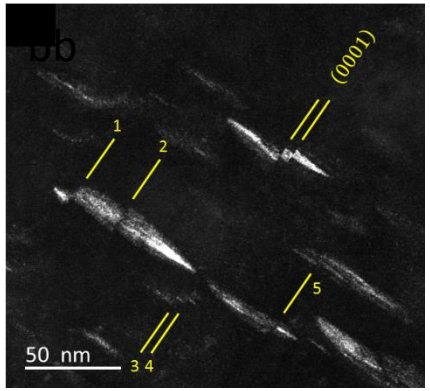

Note, peak aging may not be a transition from shearing to Orowan bowing, rather when trailing dislocations enter same precipitate as the leading.

Observation: Prismatic plate shaped β' precipitates sheared by basal <a> dislocations

Hypothesis: Flow stress controlled by precipitate order strengthening (APB energy) instead of Orowan bowing

$$\tau_{plate} = \frac{\gamma_{APB}}{2b}\left(\frac{D_p^{plate}}{\lambda_{basal}^{plate}} - f\right)$$

APB energy determined by fitting to the response of T5

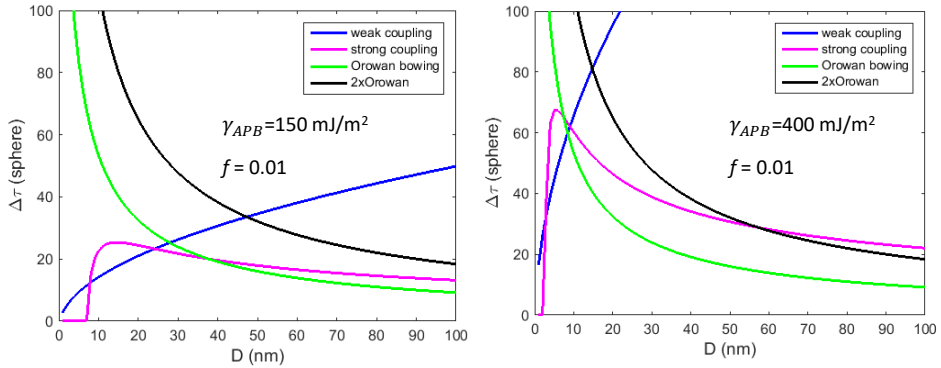

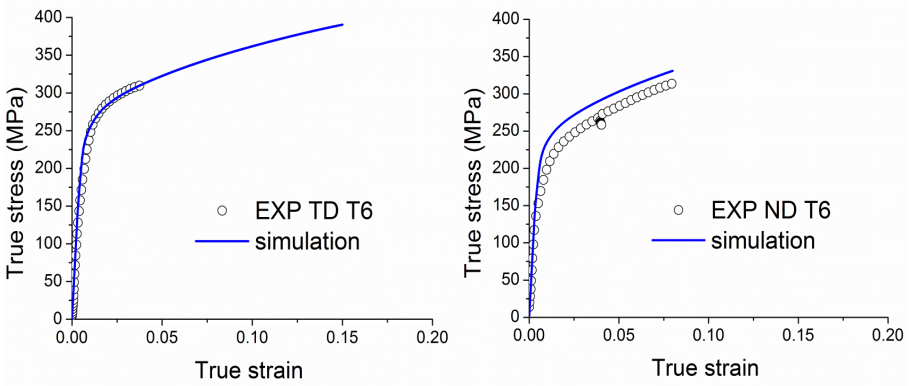

Validation: Crystal plasticity simulations trained using T5 data able to predict the flow stress during tension along TD (w/n 2%) & ND (w/n 10%) of experiments conducted on T6 (distinct grain size and texture)

T6 exhibits ductile intergranular failure due to larger precipitate free zone (PFZ) near grain boundaries

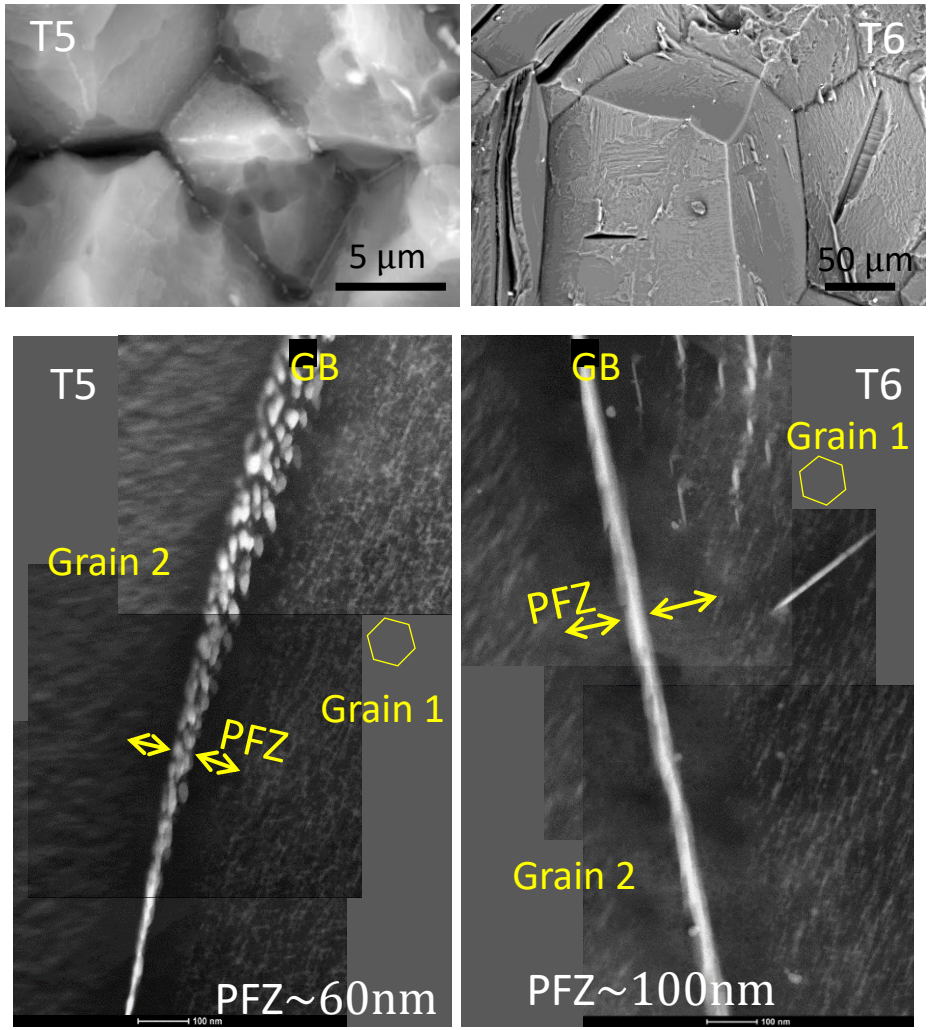

Manuscript Details

Manuscript number	INTPLA_2017_402
Title	Effect of precipitates on anisotropy - Application to aluminum alloy, 7085
Article type	Research Paper

Abstract

Commercial aluminum alloy 7085, which has been used in aerospace applications and is considered as a potential armor material, is characterized under quasistatic (0.001 /s) and high strain rate (1000 /s) uniaxial compression loading along the rolling, transverse, and normal directions (RD, TD and ND, respectively) and at 45° to RD within the plane of the plate (henceforth denoted as 45) at different aging conditions, in order to see the effect of aging on the flow stress and plastic strain anisotropy. The in-plane r-values tend towards 1, with aging, indicating that the material tends towards plastic isotropy. These results verify the previously hypothesized connection between precipitate induced-backstress and anisotropy. A model taking into account the kinematic hardening effect of an elastic inclusion within an elastoplastic single crystal has been incorporated into the elastoplastic self-consistent (EPSC) polycrystal modeling framework to quantitatively describe the effect of non-shearable precipitates on plasticity. Finally, the plastic anisotropy is shown to be remarkably sensitive to the initial texture, especially during straining along the normal direction.

Keywords	anisotropy; backstress; precipitation hardening; self-consistent; strain incompatibility; Kolsky bar.

Corresponding Author	Jishnu Bhattacharyya
Corresponding Author's Institution	University of Virginia
Order of Authors	Jishnu Bhattacharyya, Bradley Bittmann, Sean Agnew

Submission Files Included in this PDF

File Name [File Type]

Precipitates AA7085 - cover letter.docx [Cover Letter]

Precipitates AA7085 - highlights.docx [Highlights]

Effect of precipitates on anisotropy - AA7085 FINAL.pdf [Manuscript File]

Effect of precipitates on anisotropy - AA7085 FINAL.pptx [Figure]

To view all the submission files, including those not included in the PDF, click on the manuscript title on your EVISE Homepage, then click 'Download zip file'.

September 3, 2017

To the editor,

We hope that you and the reviewers find this work to be a significant addition to our current understanding of the role of precipitates on the strength and the strain anisotropy of commercial high strength Al alloys. It is an original piece of work that employs modeling supported by experimental data, to provide a detailed description of evolution of anisotropy with ageing in AA7085 alloy.

Sincerely,

Jishnu Bhattacharyya

Highlights

1. Evolution of strength and plastic strain anisotropy with ageing is measured for AA7085.
2. With ageing, the in-plane r-value tends towards 1; the material becomes more isotropic.
3. A model accounting for kinematic hardening due to non-shearable precipitates is employed.
4. The original formulation is modified to eliminate the inversion of the *ill-conditioned* grain elastoplastic stiffness.
5. The observed strain anisotropy evolution can only be explained by accounting for the backstress.

Effect of precipitates on anisotropy - Application to aluminum alloy, 7085

J. J. Bhattacharyya, B. Bittmann, and S. R. Agnew

Materials Science and Engineering, University of Virginia, Charlottesville, Virginia, U.S.A.

Abstract

Commercial aluminum alloy 7085, which has been used in aerospace applications and is considered as a potential armor material, is characterized under quasistatic (10^{-3} s^{-1}) and high strain rate (1000 s^{-1}) uniaxial compression loading along the rolling, transverse, and normal directions (RD, TD and ND, respectively) and at 45° to RD within the plane of the plate (henceforth denoted as 45) at different aging conditions, in order to see the effect of aging on the flow stress and plastic strain anisotropy. The in-plane r-values tend towards 1, with aging, indicating that the material tends towards plastic isotropy. These results verify the previously hypothesized connection between precipitate induced-backstress and anisotropy. A model taking into account the kinematic hardening effect of an elastic inclusion within an elastoplastic single crystal has been incorporated into the elastoplastic self-consistent (EPSC) polycrystal modeling framework to quantitatively describe the effect of non-shearable precipitates on plasticity. Finally, the plastic anisotropy is shown to be remarkably sensitive to the initial texture, especially during straining along the normal direction.

Keywords: anisotropy, backstress, precipitation hardening, self-consistent, strain incompatibility, Kolsky bar.

1 Introduction

Many commercial alloys are precipitation hardenable, i.e. they contain second phase particles, where their size, distribution and volume fraction can be controlled via solid state phase transformation in order to tailor the mechanical properties. The most obvious effect of such precipitates is to hinder the dislocation motion and thus increase the strength of the material. Such second phase particles also induce a composite effect, where the particles share a part of the applied stress and thus, reduce the amount of stress in the matrix. So, the matrix will flow at a larger applied stress than it would in the absence of the particles. This load sharing effect has been used extensively to model the behavior of two phase composites (for instance, Withers et al., 1989; Corbin and and Wilkinson, 1994).

Another effect, which is more subtle, is the development of strain gradients around the particles, since the matrix and the particles do not deform by the same amount. This incompatibility between the elastically (or in general, plastic with a different stiffness) deforming particle and the plastically deforming matrix, gives rise to geometrically necessary dislocations (GNDs) discussed by Ashby (1970). The isotropic hardening due to presence of these GNDs has been addressed using a Kocks-Mecking type formulation, e.g. by Estrin (1996), Cheng et al. (2003), Simar et al. (2007), and Fribourg et al., (2011). In addition to the isotropic hardening component, the storage of dislocation loops also has a directional character, which leads to kinematic hardening by exerting a 'backstress' that repels the forward motion of other dislocations on the same slip plane, but facilitates their reverse motion (e.g. Brown and Stobbs, 1971; Brown and Clarke, 1975). This kinematic contribution due to the hardening leads to Bauschinger effect (e.g., Bate et al., 1982; Caceres et al., 1996; Moan and Embury, 1979; Stoltz and Pelloux, 1976), as well as a potential

change in the relative activity of slip systems, which in turn, affects the plastic anisotropy (e.g., Bate et al., 1981).

Unlike the simple Bauschinger effect, very few studies have focused on the effect of particle-induced backstress on plastic anisotropy (Bate et al., 1981; Hosford and Zeisloft, 1972; Jobson and Roberts, 1977). For example, Bate et al. (1981) found that the strain anisotropy or *r*-value (width-to-thickness plastic strain ratio), in Al–4% Cu sheet, was strongly dependent on the aging condition. Since the crystallographic texture was largely unaffected by aging, they concluded that the precipitates were responsible for the observed it plastic anisotropy.

Several types of models have been implemented, which incorporate the effects of particles/precipitates in the description of the hardening behavior. They can be broadly classified into two categories: 1) strain gradient plasticity based models which take into account the geometrically necessary dislocations (GNDs) (Ashby, 1970) associated with the particles (for instance, Busso et al., 2000; Yassar et al., 2007) and 2) the 'elastic inclusion model', where the particle/precipitate is treated as an elastic ellipsoidal inclusion embedded in the crystalline matrix (Brown and Clarke, 1975). One advantage of the latter strategy is that it can be relatively straightforward to implement. The early applications were limited to isotropic elasticity where the particle and the matrix have same elastic constants. The model of Brown and Clarke (1975) is based on Eshelby's inclusion formalism (Eshelby, 1957) where the eigenstrain, $\boldsymbol{\varepsilon^*}$ is assumed to be equal to the unrelaxed plastic strain in the material. Thus, for an ellipsoidal inclusion with uniform eigenstrain $\boldsymbol{\varepsilon^*}$, the total strain in the inclusion $\boldsymbol{\varepsilon^{I,e}}$ is obtained according to Eshelby's solution:

$$\varepsilon_{ij}^{I} = S_{ijkl}\varepsilon_{kl}^{*} \tag{1}$$

where $\boldsymbol{S}$ is the Eshelby tensor, taking into account the shape and orientation of the ellipsoid.

Therefore, the elastic strain in the inclusion $\boldsymbol{\varepsilon}_e^I$ is given as (for small-strain deformation):

$$\varepsilon_{ij}^{I,e} = \varepsilon_{ij}^{I} - \varepsilon_{ij}^{*} = S_{ijkl}\varepsilon_{kl}^{*} - \varepsilon_{ij}^{*} = \left(S_{ijkl} - I_{ijkl}\right)\varepsilon_{kl}^{*} \quad (2)$$

Subsequently, the stress in the inclusion follows from Hooke's law:

$$\sigma_{ij}^{I} = C_{ijkl}\left(\varepsilon_{kl}^{I} - \varepsilon_{kl}^{*}\right) = C_{ijkl}(S_{klmn}\varepsilon_{mn}^{*} - \varepsilon_{kl}^{*}) = -Q_{ijkl}\varepsilon_{kl}^{*} \quad (3)$$

where $\boldsymbol{C}$ is the elastic stiffness tensor and $\boldsymbol{Q}$ is the accommodation tensor given by:

$$Q_{ijkl} = C_{ijmn}(I_{mnkl} - S_{mnkl}) \quad (4)$$

In this formulation, the value of unrelaxed plastic strain is assumed to be equal to that of the total plastic strain in the material. This is an assumption which is only valid for very small strains, where limited relaxation occurs (Brown and Clarke, 1975; Bate et al., 1981).

This 'elastic inclusion model' has been used by several researchers, e.g. (Bate et al., 1981; Brown and Clarke, 1975; Moan and Embury, 1979) to explore the role of precipitates in Al containing alloys. In recent years, it has been incorporated in phenomenological continuum plasticity models which may be used to efficiently simulate multiaxial plasticity. For instance, (Barlat and Liu, 1998 and Choi et al., 2000a) used such a model to study the simultaneous effect of texture and precipitates on plastic anisotropy in Al 4% Cu alloys. More recent attempts include incorporation within Taylor-based crystal plasticity formulations (e.g. Han et al., 2004, 2006; Anjabin et al., 2014) to study the effect of different precipitate variants and their rotation during deformation.

Although it is more computationally intensive, the crystal plasticity framework provides several advantages in comparison to phenomenological continuum models because of its inherent capability to capture anisotropic elastic and plastic properties at both the micro (grain) and macro (polycrystal) levels as well as the ability to naturally describe multiple sources of "backstress" including intergranular stresses (e.g, Mulay et al., 2011) and the presently considered intragranular

sources. Furthermore, these models are not restricted to any particular strain paths as they can take texture evolution into account.

According to the authors' knowledge, the model by Schmitt et al., 1997, later extended by Bonfoh et al., 2003, is the only attempt to implement a micromechanics-based model, which accounts for dislocation-particle interactions, in a rate-independent self-consistent crystal plasticity model. In the present work, the elastoplastic self-consistent (EPSC) model, originally developed by Turner and Tome (1994), has been modified to incorporate such a hardening formulation to evaluate the effect of precipitates on the plastic strain anisotropy of a commercial aluminum alloy, AA 7085.

2 Experimental methods

2.1 Materials, texture and microstructure

The material investigated in this study is AA 7085, provided by Alcoa (now Arconic) in three different tempers: 38.1 mm (1.5 inch) thick plate of W51 (solutionized, quenched and stretched to relieve residual stress, followed by natural aging, unintentional and due to the unstable nature of the quenched state); 40.64 mm (1.6 inch) thick plate of T711 (slightly over-aged to enhance ballistic resistance (Doherty et al., 2012)); and 52.4 mm (2.06 inch) thick T721 (significantly over-aged to enhance blast resistance (Doherty et al., 2012)). Additionally, solution heat treatment (T3) was carried out in an air furnace at 470 °C for 1 hour. The temperature was maintained within ± 2 °C. The specimens were quenched in water at room temperature. Some of the solutionized specimens were then peak-aged (T6) at 120 °C for 24 hours.

In an earlier study (Bhattacharyya et al., 2017), it was found that there was a texture gradient along the through thickness direction of the plates. Furthermore, it was found that the plastic anisotropy, especially along the ND, was very sensitive to the initial texture. Hence, all the

specimens investigated in this study were extracted from the midplane of the plates. The procedure used to measure the texture using X-ray diffraction has been described in detail elsewhere (Bhattacharyya et al., 2016). In brief, the {111}, {200}, and {220} incomplete ($\chi = 0^o$ to 80^o) pole figures were obtained. These data were analyzed using MTeX (Hielscher and Schaeben, 2008) to generate complete orientation distributions (ODs) and full pole figures. The pole figures collected from the midplane for T3 and T721 material are shown in Fig. 1. They are quite similar to T711 (Bhattacharyya et al., 2017) and W51, though there are fine-scale differences in the strength of the different texture components.

To quantify these subtle differences in texture among the different tempers, the volume fractions of individual orientations were obtained using MTeX, by integrating the product of the ODF and a Gaussian function centered on the considered orientation with a spread of 20^o (Table 1). As expected, the T3 temper shows the highest amount of recrystallization components (Cube and Goss) due to the solutionizing heat treatment.

Table 1: Volume fraction of texture components at midplane for T721, W51 and T3 tempers calculated with 20^0 breadth (triclinic symmetry)

Name	Indices	Bunge (φ_1 Φ φ_2)	T721	W51	T3
Copper	{112}<11$\bar{1}$>	90° 30° 45°	9	4	9
S	{123}<63$\bar{4}$>	59° 34° 65°	16	15	17
Brass	{110}<$\bar{1}$12>	35° 45° 0/90°	25	33	27
Cube	{100}<001>	0° 0° 0/90°	8	11	9
Goss	{110}<001>	0° 45° 0/90°	3	2	6
β-fibre/Rxx			4.5	4.0	3.5

If one considers the ratio of the volume fractions of the deformation texture (β-fibre: Copper, S and Brass) components to that of the recrystallization (Cube and Goss) components, the strong resilience of the texture of this material against annealing is further evident; emphasizing the fact that these alloys are highly resistant to recrystallization. However, it will be shown that these slight texture differences do lead to quantifiable variation in the plastic strain anisotropy along the ND.

2.2 Mechanical testing

The plastic strain anisotropy is assessed by measuring the compressive r-values along three orthogonal directions, following the convention of Jain and Agnew (2007):

$$r_{RD} = \varepsilon_{TD}/\varepsilon_{ND} \quad (5a)$$

$$r_{TD} = \varepsilon_{RD}/\varepsilon_{ND} \quad (5b)$$

$$r_{ND} = \varepsilon_{TD}/\varepsilon_{RD} \quad (5c)$$

The r-value along the 45direction is defined as:

$$r_{45} = \varepsilon_{-45}/\varepsilon_{ND} \quad (5d)$$

where ε_{-45} is the strain orthogonal to the axial and through thickness directions.

Compression specimens, in the form of right circular cylinders of 8mm diameter and height, were wire electrical discharge machined (EDM'd) from the plate along RD, TD, ND, and 45 directions. Uniaxial compression tests at a strain rate of 10^{-3} s^{-1} were performed using a universal testing machine, and the axial strain was measured using a laser extensometer. The laser extensometers tags were not directly attached to the sample. Hence, the recorded force-displacement data included the machine compliance, which was removed following standard procedures (e.g., Follansbee, 2014). Typically 3-4 specimens for a given condition were tested to examine sample-to-sample variation, but only one representative flow curve is presented, for ease

of reading. The results for all the tempers were found to be quite consistent. To measure the evolution of r-value with strain, the samples were unloaded at specific strain levels, typically after 5% increments, and the strains along the transverse and thickness directions were measured using a digital caliper. Volume constancy ($\varepsilon_{ii} < 0.001$) was enforced to ensure accurate measurements. Fractured samples were not used to assess the r values because they exhibit inhomogeneous strain.

A split Hopkinson pressure (or Kolsky) bar testing apparatus was used to assess the uniaxial compression behavior along RD, ND and transverse direction (TD) at a nominal strain rate of 1250 s^{-1}, following procedures described earlier ((Agnew et al., 2014; Bhattacharyya et al., 2016). The actual strain rates varied from 1100-1400 s^{-1}. To ensure near constant strain rates, cylindrical pulse shapers of 10 mm diameter and 1 mm length cut from AA1100 alloy were used. This also helps to eliminate the high frequency Pochhammer-Chree oscillations, due to dispersion in the flow curve (Gray, 2000; Chen and Song, 2010). The condition for stress equilibrium was checked during data processing to ensure uniform loading of the specimen. The r-values under dynamic loading conditions were measured at a single imposed strain level instead of multiple intermediate strain levels like the quasistatic. Finally, the apparent strain rate sensitivity m is calculated at 2% offset strain, using the relation:

$$m = \frac{\partial ln\sigma(\varepsilon)}{\partial ln\dot{\varepsilon}} = \frac{\ln\left(\frac{\sigma_2}{\sigma_1}\right)}{\ln\left(\frac{\varepsilon_2}{\varepsilon_1}\right)} \quad (6)$$

3 Modeling

3.1 The EPSC model

The relevant equations of the original EPSC model are highlighted, to facilitate comparison with the modified model. The details of the original model are given in (Hutchinson, 1970; Turner and Tomé, 1994). A ‘grain’ represents a collection of physical grains having a particular orientation, with a volume fraction commensurate with the experimentally measured texture, and

is approximated as an anisotropic elastoplastic ellipsoidal inclusion. This grain is embedded in an anisotropic homogeneous effective medium (HEM), which represents the polycrystalline aggregate. The grain level and aggregate level response are connected using a modified Eshelby equivalent inclusion formalism.

3.1.1 Grain level constitutive behavior

Under isothermal conditions and restriction to small strains*, the constitutive relation of a grain (or crystal) *c*, is given by the differential form of Hooke's law, relating the stress increment $\boldsymbol{d\sigma^c}$ to the *elastic* strain increment:

$$d\sigma_{ij}^{c} = C_{ijkl}^{c} : \left[d\varepsilon_{ij}^{c} - \sum_s m_{ij}^{\alpha} \, d\gamma^{\alpha} \right] \quad (7)$$

where, $\boldsymbol{C^c}$ is the elastic stiffness tensor of the crystal *c*, $\boldsymbol{d\varepsilon^c}$ is the total strain increment in crystal *c*, and the total plastic strain increment is given by $\sum_{\alpha} m_{ij}^{\alpha} \, d\gamma^{\alpha}$; i.e. shear increment $d\gamma^{\alpha}$ on slip system α, resolved by the Schmid tensor $\boldsymbol{m}^{\alpha}$ and summed over all active slip systems. In order to use the Eshelby formalism, the constitutive relation (Eq. 7) has to be linearized. The linearization procedure and the self-consistent formulation have been described in detail elsewhere ((Hutchinson, 1970; Neil et al., 2010; Turner and Tomé, 1994).

For a slip system to be potentially active it should satisfy the Schmid law, $m_{ij}^{\alpha}\sigma_{ij}^{c} = \tau_{cr}^{\alpha}$. Moreover, the system has to remain loaded and satisfy the consistency condition, $m_{ij}^{\alpha} d\sigma_{ij}^{c} = d\tau_{cr}^{\alpha}$, i.e. the stress has to remain on the yield surface throughout the straining step, while the yield surface evolves due to strain hardening (Hill, 1965). The evolution of the CRSS, $d\tau_{cr}^{\alpha}$ is dependent on the shear rates of all active slip systems and is given by (Hill, 1966): $d\tau_{cr}^{\alpha} = V^{\alpha}(\Gamma) h^{\alpha\beta} d\gamma^{\beta}$, where $h^{\alpha\beta}$ is the latent hardening matrix that defines how much slip in system α hardens slip

* Note: Although the model is implemented for the small strain case, the grain-level crystal-plasticity concepts discussed here can readily be extended to the finite strain case.

system β, and $V^{\alpha}(\Gamma)$ is empirical Voce strain hardening rule which determines the evolution of the current threshold stress, starting from an initial threshold stress τ_0^{α}, $:V^{\alpha}(\Gamma) = \frac{\partial \tau_v^{\alpha}}{\partial \Gamma} = \theta_0^{\alpha}\left(1 - \left(\frac{\tau^{\alpha} - \tau_0^{\alpha}}{\tau_1^{\alpha}}\right)\right).\Gamma = \sum_{\alpha} \gamma^{\alpha}$ is the total shear strain in a grain, τ_v^{α} is the current threshold strength of system α, $\tau_0^{\alpha} + \tau_1^{\alpha}$ is the saturation stress, and θ_0 is the initial strain rate. Thus, there are three fitting parameters per slip mode. Notably, Kocks and Mecking (2003) describe how the Voce-type slip system level hardening rule can be related to dislocation theory.

3.1.2 Grain with elastic particles

In the following subsections, a constitutive model for a composite grain containing elastic particles, based on the formulation by Schmitt et al., (1997) and Bonfoh et al., (2003) is described. In their original formulation, they rely upon the elastoplastic compliance of the equivalent heterogeneous grain, $(\boldsymbol{L}^c)^{-1}$, computed by inverting the stiffness tensor. This is problematic because the grain elastoplastic stiffness $\boldsymbol{L}^c$ decreases with strain, especially for the aged specimens, where even the polycrystal response is almost perfectly plastic. The reduction in the stiffness value is drastic; starting from the elastic stiffness of ~ 70 GPa it reduces to less than 100 MPa, i.e., by almost 3 orders of magnitude. This makes the stiffness matrix very *ill-conditioned* and virtually impossible to invert without introducing large numerical errors. In order to avoid this problem, the equations are reformulated to eliminate the need to invert the grain stiffness as $(\boldsymbol{L}^c)^{-1}$. Additionally, the formulation is modified to take into account the relaxation of the backstress, in a way similar to that suggested by Barlat et al., (Barlat and Liu, 1998; Choi et al., 2000b).

3.1.3 The heterogeneous grain

Given the volume fraction of particles (e.g., precipitates) is *f*, the total strain increment in a grain $\boldsymbol{d\varepsilon}^c$ may be partitioned between the matrix (elastoplastic) and the precipitate (elastic)

according to a simple rule of mixtures. If the particle is assumed to be elastic[†], the total plastic strain increment of the heterogeneous grain is only due to that in the matrix. Using Hooke's law one obtains:

$$d\varepsilon_{ij}^{c} = fC_{ijkl}^{ppt\,-1} d\sigma_{kl}^{ppt} + (1-f)L_{ijkl}^{m}{}^{-1} d\sigma_{kl}^{m} = fC_{ijkl}^{ppt\,-1} d\sigma_{kl}^{ppt} + (1-f)\left(C_{ijkl}^{m}{}^{-1} d\sigma_{kl}^{m} + d\varepsilon_{ij}^{m,pl}\right) \quad 8)$$

where, $\boldsymbol{d\varepsilon}^{ppt}$, $\boldsymbol{d\sigma}^{ppt}$ and $\boldsymbol{C}^{ppt}$ are the incremental total (elastic only) strain, stress and elastic stiffness of the particle, respectively, and $\boldsymbol{d\varepsilon}^{m}$, $\boldsymbol{d\varepsilon}^{m,el}$, $\boldsymbol{d\varepsilon}^{m,pl}$, $\boldsymbol{d\sigma}^{m}$, $\boldsymbol{C}^{m}$ and $\boldsymbol{L}^{m}$ are the incremental total, elastic and plastic strain, stress and elastic and elastoplastic stiffness of the matrix respectively. Thus, the plastic strain increment of the heterogeneous grain is given by:

$$d\varepsilon_{ij}^{c,pl} = (1-f)\sum_{\alpha} m_{ij}^{\alpha}\, d\gamma^{\alpha} = \sum_{\alpha} m_{ij}^{\alpha}\; d\gamma^{\alpha,c} \text{ where, } d\gamma^{\alpha,c} = (1-f)d\gamma^{\alpha} \quad (9)$$

The total stress increment $\boldsymbol{d\sigma}^{c}$ can be written using the rule of mixtures:

$$d\sigma_{ij}^{c} = fd\sigma_{ij}^{ppt} + (1-f)d\sigma_{ij}^{m} \quad (10)$$

from which the matrix stress can be obtained as:

$$d\sigma_{ij}^{m} = \frac{d\sigma_{ij}^{c} - fd\sigma_{ij}^{ppt}}{1-f} \quad (11)$$

3.1.4 Yield criteria for the heterogeneous grain

A slip system within the matrix of the equivalent grain is potentially active once the resolved shear stress $\tau^{\alpha,m}$ is equal to the CRSS of that system. That is:

[†] Again, this is an assumption which may be relaxed to better describe the response of alloys with shearable precipitates. Here, an approximation is introduced to account for the possibility of plastic relaxation of any sort, later in the formulation.

$$\tau^{\alpha,m} = m_{ij}^{\alpha}\sigma_{ij}^{m} = \tau_{CRSS,m}^{\alpha} \quad (12)$$

where, $\tau_{CRSS,m}^{\alpha}$ is the critical resolved shear stress of the matrix. Substituting Eq. (11) into (12) gives:

$$m_{ij}^{\alpha}\left(\sigma_{ij}^{c} - f\sigma_{ij}^{ppt}\right) = (1-f)\tau_{CRSS,m}^{\alpha} = \tau_{CRSS,c}^{\alpha} \quad (13)$$

where $\tau_{CRSS,c}^{\alpha}$ is now the CRSS of the heterogeneous grain. Comparing with the homogeneous single crystal case, the yield function for the heterogeneous grain now includes a 'backstress', $f\sigma^{ppt}$. This provides kinematic hardening in addition to any regular hardening term incorporated in $\tau_{CRSS,c}^{\alpha}$, which can itself be anisotropic (e.g., through a latent hardening matrix).

As discussed above, the particles induce strain incompatibilities, which result in a mismatch between the stress increment in the equivalent grain and that in the matrix. The matrix stress increment can be expressed as:

$$d\sigma_{ij}^{m} = d\sigma_{ij}^{c} + P_{ijkl}^{c} d\varepsilon_{kl}^{m} \quad (14)$$

where, $\boldsymbol{P}^{c}$ is a polarization tensor, and $\boldsymbol{P}^{c}$: $\boldsymbol{d\varepsilon}^{m}$describes the stress increments due to the strain incompatibility (Schmitt et al., 1997; Bonfoh et al., 2003). Thus, the consistency condition takes the form:

$$m_{ij}^{\alpha}\left[d\sigma_{ij}^{c} + P_{ijkl}^{c}\left({C_{ijkl}^{m}}^{-1} d\sigma_{kl}^{m} + \sum_{\alpha} m_{ij}^{\alpha}\, d\gamma^{\alpha}\right)\right] = \sum_{\beta} V^{\alpha}(\Gamma) h^{\alpha\beta}\, d\gamma^{\beta} \quad (15)$$

For convenience, all the variables are expressed in terms of the particle and the grain quantities. The same has to be done with $d\sigma_{kl}^{m}$, as shown in the Appendix. The final expression for the consistency condition is obtained as:

$$m_{ij}^{\alpha}\left[(1-f)I_{ijuv}+P_{ijkl}^{c}\,{C_{klmn}^{m}}^{-1}\left(I_{mnuv}-fC_{mnrs}^{ppt}T_{rsxy}^{ppt}\left(L_{xyuv}^{c}\right)^{-1}\right)\right]d\sigma_{uv}^{\alpha}$$

$$=\sum_{\beta}\left(V^{\alpha}(\Gamma)h^{\alpha\beta}-m_{ij}^{\alpha}\,P_{ijkl}^{c}\,m_{kl}^{\alpha}\right)d\gamma^{\beta,c} \quad (16)$$

where $\boldsymbol{T^{ppt}}$ is the strain concentration tensor relating the strain increment of the precipitate to that of the grain (see Appendix):

$$T_{ijkl}^{ppt}=\left(C_{ijop}^{ppt}+\,L_{ijop}^{*}\right)^{-1}\left(L_{opkl}^{c}+\,L_{opkl}^{*}\right) \quad (17)$$

where $L_{ijmn}^{*ppt}=L_{ijkl}^{c}\left({S_{klmn}^{ppt}}^{-1}-\,I_{klmn}\right)$. In this equation, $\boldsymbol{S}^{ppt}$ is the Eshelby tensor for the particle, which depends on the particle shape (e.g. disc, rod, sphere) and orientation with respect to the surrounding grain crystallographic coordinates (which can be used to specify orientation relationships). If one defines the increase in the critical resolved shear strength $d\tau_{CRSS,c}^{\alpha}$ using a latent hardening matrix $H^{\alpha\beta}$ as:

$d\tau_{CRSS,c}^{\alpha}=\sum_{\beta}H^{\alpha\beta}\,d\gamma^{\beta,c}$ where (18)

$$H^{\alpha\beta}=V^{\alpha}(\Gamma)h^{\alpha\beta}-m_{ij}^{\alpha}\,P_{ijkl}^{c}\,m_{kl}^{\beta} \quad (19)$$

and another fourth rank tensor, $\boldsymbol{U}$ as:

$$U_{xyop}=(1-f)I_{xyop}+P_{xyab}^{c}(C_{abuv}^{c})^{-1}\left(I_{uvop}-fC_{uvij}^{ppt}\,\left(L_{ijop}^{c}+S_{ijmn}^{ppt}\left(C_{mnop}^{ppt}-\,L_{mnop}^{c}\right)\right)^{-1}\right) \quad (20)$$

The final consistency condition for the heterogeneous grain can be expressed compactly as:

$$m_{ij}^{s}U_{ijuv}d\sigma_{uv}^{c}=\sum_{\beta}H^{\alpha\beta}\,d\gamma^{\beta,c} \quad (21)$$

The hardening behavior of each slip system, $H^{\alpha\beta}$, is now a function of both the Voce hardening term (including latent hardening effects), which is modified by the polarizing (kinematic) effect of the precipitates, through the tensor $\boldsymbol{P}$. The tensor $\boldsymbol{U}$ includes the influence of precipitates through $\boldsymbol{S}^{ppt}$ and $\boldsymbol{P}^{c}$, as well as the instantaneous elastoplastic stiffness of the heterogeneous grain, $\boldsymbol{L}^{c}$. The

derivation for the tensor $\boldsymbol{P}^c$ has been discussed in detail by Bonfoh et al., (2003). The expression for $\boldsymbol{P}^c$ in terms of the strain concentration tensor $\boldsymbol{T}^{ppt}$ can be obtained as (see Appendix):

$$P^c_{ijop} = f\left(L^c_{ijop} - C^{ppt}_{ijuv}T^{ppt}_{uvmn}\right)\left(I_{mnop} - fT^{ppt}_{mnop}\right)^{-1} \tag{22}$$

3.1.5 Constitutive relation of the equivalent grain

Assuming the elastic stiffness of the precipitate and the matrix are equal i.e. $\boldsymbol{C}^{ppt} = \boldsymbol{C}^m = \boldsymbol{C}^c$, then the total strain in the grain (Eq. 8) simplifies to:

$$d\varepsilon^c_{ij} = {C^c_{ijkl}}^{-1} d\sigma^c_{kl} + (1-f)\left(d\varepsilon^{m,pl}_{kl} = \sum_\alpha m^\alpha_{kl}\, d\gamma^\alpha\right) \tag{23}$$

Thus, the constitutive relation for the heterogeneous grain becomes:

$$d\sigma^c_{ij} = C^c_{ijkl}\colon [d\varepsilon^c_{kl} - \sum_\alpha m^\alpha_{kl}\, d\gamma^{\alpha,c}] = C^c_{ijkl}\colon \left(d\varepsilon^c_{kl} - d\varepsilon^{c,pl}_{kl}\right) \tag{24}$$

which is linearized in the usual way:

$$d\sigma^c_{ij} = L^c_{ijkl}\colon d\varepsilon^c_{kl} \tag{25}$$

where $\boldsymbol{L}^c$ is now the instantaneous elasto-plastic stiffness tensor of the equivalent grain *c*. Using Eq. (24) and Eq. (25), $\boldsymbol{L}^c$ can be obtained as:

$$L^c_{mnkl} = C^c_{mnij}\left(I_{ijkl} - \sum_\alpha m^\alpha_{ij}\, {Q_{kl}}^\alpha\right) \tag{26}$$

where, $$d\gamma^{\alpha,c} = {Q_{ij}}^\alpha {d\varepsilon_{ij}}^\alpha \tag{27}$$

This $\boldsymbol{Q}$ tensor relates the shear increments of the equivalent grain in terms of the imposed strain increments. By substituting Hooke's law into the consistency condition (Eq. 23) one obtains,

$$m^\alpha_{ij}U_{ijuv}C^c_{uvmn}\,[d\varepsilon^c_{mn} - \sum_\alpha m^\alpha_{mn}\, d\gamma^{\alpha,c}] = \sum_\beta H^{\alpha\beta}\, d\gamma^{\beta,c} \tag{28}$$

Which upon rearranging, simplifying and denoting $X^{\alpha\beta} = \left(m^\alpha_{ij}U_{ijuv}C^c_{uvmn}m^\beta_{mn} + H^{\alpha\beta}\right)$ we get,

$$d\gamma^{\beta,c} = \sum_\beta (X^{-1})^{\alpha\beta}\, m^\beta_{ij}U_{ijuv}C^c_{uvmn}\, d\varepsilon^c_{mn} \tag{29}$$

Comparing Eq. (28) and Eq. (30),

$$Q^{\alpha}_{mn} = \sum_{\beta}(X^{-1})^{\alpha\beta}\, m^{\beta}_{ij} U_{ijuv} C^{c}_{uvmn} \tag{30}$$

The form of these expressions (Eq. 29 and Eq. 30) are very similar to those used in the original EPSC model (Tome et al., 2002) and hence can be implemented with minimal change in the structure of the code.

Finally, the heterogeneous grain elastoplastic stiffness (Eq. 26) becomes:

$$L^{c}_{ijmn} = C^{c}_{ijpq}\left(I_{pqmn} - \sum_{\alpha} m^{\alpha}_{pq} \sum_{\beta}(X^{-1})^{\alpha\beta} m^{\beta}_{pq} U_{pquv} C^{c}_{uvmn}\right) \tag{31}$$

This expression replaces the homogenous single crystal elastoplastic stiffness in the original EPSC model; subsequently the standard self-consistent homogenization between this heterogeneous grain and the effective medium is carried out.

3.1.5.1 Incorporating relaxation effects

The polarization tensor $\boldsymbol{P^c}$ takes into account the strain mismatch that is generated between the elastic particle and the elastoplastic matrix. Now, the evolution of $\boldsymbol{P^c}$ with straining is governed by the instantaneous elastoplastic stiffness of the grain, as well as the strain concentration tensor $\boldsymbol{T}^{ppt}$. Physically, this takes into account the effect of dynamic recovery that determines the net accumulation of dislocations, and hence the strain hardening rate, (in the form of the Voce hardening law). However, in the presence of the particles, there is an additional recovery which takes place, as observed experimentally (e.g., Brown and Stobbs, 1971; Atkinson et al., 1974), and the present formulation does not account for this. Thus, a final modification is accounting for the relaxation of the strain/stress concentration due to these physical phenomena.

Previous experiments (Wilson, 1965; Moan and Embury, 1979; Bate et al., 1982) show that the effect of particle-induced internal stress is prominent only for a few percent strain, after which it saturates. The generally accepted physical explanation is that there is a maximum number of dislocation loops that can accumulate around a particle, which is proportional to size of the

particle (Ashby, 1970). Before this critical number of loops is achieved, the stress due to the pile up increases and once the limit is reached, several things can happen; the particle can shear, the particle-matrix interface can de-bond or the stress concentration can activate secondary slip systems or produce prismatic loops, all of which relax the stress that developed due to the pile up (Brown and Stobbs, 1971, 1976; Brown and Clarke, 1975) . Barlat and Liu, (1998b) and Choi et al., (2000) have applied a simple exponential decay function to the backstress in their continuum models, to capture the effect of such relaxation mechanisms. Interestingly, Proudhon et al., (2008) derived an experimentally motivated analytical model for the evolution of the unrelaxed plastic strain with applied strain, and came up with an exponential relationship. Thus, an exponential decay term is, for simplicity, assumed to be a function of the equivalent strain of the heterogeneous grain, is multiplied to the strain concentration tensor derived earlier as:

$$T_{ijkl}^{ppt} = \left(C_{ijop}^{ppt} + L_{ijop}^{*}\right)^{-1}\left(L_{opkl}^{c} + L_{opkl}^{*}\right)\exp\left(-\frac{\varepsilon_{VM}^{c,p}}{\varepsilon_{sat}}\right) \quad (32)$$

where, $\varepsilon_{VM}^{c,p}$ is the Von-Mises equivalent *plastic* strain in the heterogeneous grain *c*, and ε_{sat} is the saturation stress value which can, in principle, be obtained from Bauschinger tests. This way, although the relaxation behavior is accounted for empirically, there are no arbitrary fitting parameters involved in the model, each has a specific physical meaning.

3.2 Simulation methodology

In an earlier study, it was found that the r-values along TD and ND were highly sensitive to the texture. For simplicity of presentation, as well as keeping in mind the goal of capturing the observed trends, only the midplane textures have been used in the simulations. The individual textures for W51 and T721 tempered samples were discretized as 2000 "grains" appropriately oriented and volume weighted, in order to match the experimentally observe texture. In order to simplify the application of the uniaxial stress boundary conditions for the 45° orientation

specimens, the textures were first rotated by 45° about ND. The interaction strength between the grains and the medium can be modified empirically by changing a β parameter ($0.5 \leq \beta \leq 1$) in the interaction equation:

$$\left(d\sigma_{ij}^{c} - d\sigma_{ij}\right) = -\beta L_{ijkl}^{*}\left(d\varepsilon_{kl}^{c} - d\varepsilon_{kl}\right) \quad (33)$$

where $\boldsymbol{L^*}$ is called the interaction stiffness, and is given by: $L_{ijkl}^{*} = L_{ijmn}\left(S_{mnkl}^{-1} - I_{mnkl}\right)$. Tension-compression (Bauschinger) tests, carried out on T3 material, showed only a small Bauschinger effect, indicating the presence of very low intergranular residual stresses which implies a very compliant interaction between the grains. Based on this fact, the β parameter was set to 0.5; the lowest value of β for which EPSC remains numerically stable (Mulay et al., 2011).

For simplicity and computational efficiency, the particles were assumed to be spheres; with cube-on-cube orientation relationship, with respect to the crystal coordinate system of the surrounding grain. It is noted that 7000 series alloys contain precipitates (η' and η) which are typically plate shaped as well as spherical Al_3Zr dispersoids (Park and Ardell, 1983; Srivatsan et al., 1997). Even though the formulation is completely general, and can treat any arbitrarily shaped ellipsoid on any given habit plane, accounting for the different variants is non-trivial, especially for a commercial alloy where different shaped precipitates/dispersoids with different orientation relationships are present. Furthermore, it is computationally expensive because the Eshelby tensor $\boldsymbol{S}^{ppt}$ as well as the strain concentration relations have to be calculated for each variant and averaged in an appropriate manner. It is acknowledged that this simplifying assumption (of a single spherical variant) would affect the results quantitatively, however, the qualitative trends are expected to remain the same. Furthermore, the actual precipitate volume fraction for the different tempers were not measured, rather a plausible precipitate volume fraction of 0.05 is chosen for the simulations, in keeping with prior observations of similar alloys (Deschamps et al., 2001; Dumont

et al., 2004, 2005). Note that the main strengthening effect of shearable and non-shearable precipitates is already accounted for by the level of the critical resolved shear stress for dislocation motion. It is only the secondary backstress effects which are related to the present Eshelbian approach.

Uniaxial straining increments of 10^{-4} were imposed parallel to the loading direction while the shear strains and normal stresses along the two directions perpendicular to the loading direction were set to zero. The other components of stresses and strains were unknown. These boundary conditions allowed the natural development of lateral strains used to compute the r-values. Since the effect of the backstress is only dominant for the first few percent of strain, all the simulations were restricted to <10% strain. Moreover, since the formulation is based on small strain assumptions, texture evolution was not considered in any of the cases. The effect of texture evolution during large strain deformation was already considered using VPSC modeling in an earlier publication (Bhattacharyya et al., 2017). At the risk of redundancy, the present work is concerned with exploring the possibility that discrepancies between those prior VPSC simulations and experiments were due to neglect of precipitate-induced backstresses.

4 Results

The experimental data presented in this section are organized as follows. In order to see the effect on strength anisotropy with aging, the flow curves at 10^{-3} s^{-1} and at ~1000 s^{-1} along different loading directions for each temper investigated is presented first. Next, to elucidate the variation of plastic strain anisotropy with aging, the r-values for each loading direction are presented.

4.1 Flow behavior

The flow curves at 10^{-3} s^{-1} for T3 and T6 material are shown in Figure 2a. The dramatic age-hardening response is evident, T3 solutionizing treatment dissolved the fine dispersion of strengthening precipitates present in the as-received material and the T6 (peak-aged) condition. The T3 temper shows a protracted elastoplastic transition and there is nearly no yield strength anisotropy; for all the directions, the yield strength is 270 ± 20 MPa. All directions exhibit good strain hardening capacity, however, it is different for different directions. The 45 direction shows the highest strain hardening followed by TD and ND, while the RD has the lowest hardening rate. The TD and ND tend to show saturation in strain hardening at ~ 30% strain. On the other hand, the T6 temper shows a large yield strength anisotropy: the yield strength along RD and TD is ~ 550 MPa, whereas along ND and 45 it is ~ 475 MPa. The yielding behavior, especially for RD and TD, is sharp as compared to the T3 material. The hardening behavior is typical for peak-aged precipitation strengthened Al alloys (e.g., Cheng et al., 2003), the strain hardening capacity is greatly diminished for RD and TD, while the ND and 45 still show moderate hardening behavior. Notably, none of the T3 and T6 specimens failed up to 30% strain, which is in contrast with the T711 temper, where catastrophic shear failure was observed (Bhattacharyya et al., 2017). The flow curves at 1000 s^{-1} are shown in Figure 2b. The hardening rates saturate after about 15% strain for all the directions investigated. The flow stress anisotropy is different at high strain rate, with RD showing higher yield than TD and ND.

For the specimen which was solutionized, stretched for stress-relieving and subsequently naturally aged, (W51) the flow curves show slight yield anisotropy, where RD, TD and ND have yield strength of ~ 450 MPa, whereas the 45 has a lower yield strength of ~ 400 MPa (Figure 3a). The discontinuities in the flow curves are due to the interruptions required to make r-value

measurements. The strain hardening rate overall is lower than the T3 but higher than T6. The TD, ND and 45 show a higher strain hardening rate than RD, which is similar to the trend observed for both T3 and T6. In all these three tempers, loading along the 45 direction shows the highest strain hardening capacity, often exceeding the flow stress along RD after ~ 10-15% strain, albeit having a lower yield strength. Only TD tends to exhibit saturation in strain hardening after ~25% strain and the ND specimen exhibited shear fracture after only ~16 % compressive strain.

Figure 3b shows the flow curves at dynamic strain rates for the W51 material. In this case, the ND and TD have the highest yield strength and flow stress, while the RD and 45 is lower. The hardening rates of ND and 45 are similar and greater than TD, while the RD is the lowest. The dynamic data show very similar trends as observed in the quasistatic case, indicating that the flow strength anisotropy does not exhibit obvious strain rate dependence. Given that there is a single, dominant mechanism of plastic deformation (octahedral slip), this is not surprising.

The RD, TD and ND data for T711 temper have been published in an earlier study (Bhattacharyya et al., 2017), however the 45 data is new. The flow curves for all the directions are shown in Fig. 4 for the ease of comparison. Similar to W51 temper, the ND and the TD exhibit the highest yield strength while the 45 has the lowest (Figure 4a). The trends in strain hardening rate are also very similar to W51, with 45 showing the highest hardening rate among all four directions. The RD, TD and 45 show good compressive ductility, exhibiting no failure up to ~40% strain, unlike most ND specimens which fractured abruptly after ~25% strain. It is of interest to note that the magnitude of yield strength, flow stress, strain hardening rate and the level of strength anisotropy are very similar to that of the T6 temper. This is due to the fact that this temper is very close to the peak-aged condition, the essential difference being the stretch it received for stress-

relieving. The dynamic data (Figure 4b) also shows similar trends as the quasistatic; 45 direction shows the highest hardening rate.

Upon further aging, to create the T721 temper, the strength of the material decreases (Figure 5). There is very little yield anisotropy between RD, TD and ND. None of the specimens failed up to ~20% strain. The yield strength for all the directions is ~ 400 MPa. The strain hardening behavior is quite different for this temper. Notably, the 45 specimens exhibits a lower hardening rate than the other three directions. Along all the directions, the specimens exhibit rapid strain hardening up to ~ 10% strain followed by saturation and almost perfect plastic behavior. This type of flow behavior is typical of non-shearable precipitate containing materials, where the initial rapid strain hardening is attributed to the buildup of internal stresses around the precipitates and once these stresses relax, the strain hardening rate decreases (Cheng et al., 2003; Poole et al., 2007).

Under dynamic conditions, (Figure 5b), the flow curves exhibit flow softening after 10% strain. This is expected since the material exhibited quite low strain hardening at the quasistatic strain rate. Flow localization, due to near adiabatic conditions experienced under dynamic loading, is likely to start at earlier stages, in the absence of strain hardening. Like the other tempers, the flow strength shows slight positive rate sensitivity (Table 2) and the strength anisotropy remains the same.

The values presented in Table 2 show slight negative strain rate sensitivity for the T3 material, probably because of the low strain hardening at dynamic rates. Another possibility for the observed negative rate sensitivity is dynamic strain ageing. Recall that the solutionized material has a larger solute content in the matrix, and the effect of solutes interacting with mobile and forest dislocations can lead to dynamic strain ageing (e.g., Kubin and Estrin, 1991). In fact,

the increasing strain rate sensitivity with aging is consistent with the decreasing level of solute content in the matrix. For all the other tempers, the rate sensitivity is quite low and positive, and thus using a rate independent model to describe their constitutive behavior is deemed appropriate.

Table 2: Values of strain rate sensitivity *m* calculated from RD flow curves, with stress values at 2% offset

Temper	*m* (2% offset)
T3	-0.005
W51	0.003
T711	0.002
T721	0.008

4.2 Plastic strain anisotropy (r-value)

The r-values along RD for all the tempers investigated are much less than 1 (Figure 6a), indicating low thinning resistance, which is common in rolled Al alloy plates and sheets. However, there is a variation in the r-values among the tempers. For the T3 material, lowest r-values are observed; starting from ~ 0.18 at plastic strains < 5% they gradually increase up to 0.3 and apparently saturate. The naturally aged W51 shows a similar trend with values that are only slightly higher than that of T3. It starts from ~ 0.25 and gradually rises to 0.35 after about 25% strain. The T6 and T711 material, on the other hand, exhibit higher r-values of 0.35 which essentially remain constant with straining. The most interesting behavior is exhibited by the overaged T721 material where it starts from ~0.25 at early stages of deformation but rapidly increase to ~0.5 within 20% strain. These results suggest that the magnitude and the evolution of the r-values with strain is temper dependent. The r-values at dynamic strain rates show a similar trend, although they appear to be slightly lower (at a given strain level) as compared to their quasistatic counterparts.

The r-values along TD for all the tempers are also less than 1 but greater than the values for RD (Figure 6b). The r-values of the overaged tempers (T711 and T721) tend to be higher (closer to 1) than T3, W51 and T6 tempers. Unlike RD, the TD r-values for all the tempers show a steady increase with strain. For the T3 material, r-values starting from ~ 0.4 at plastic strains < 5% increase up to 0.7 at ~ 25% strain. The naturally aged W51 again follows the T3 trend in general. There is essentially no difference in the r-values for the W51 and the T6 material; both exhibiting r-values of 0.6-0.7 within the strain range investigated. The r-value for T711 remains quite constant at ~ 0.8 throughout straining whereas, the overaged T721 material the r-value for starts from ~0.6 and steadily increases to ~0.8 within 20% strain.

The r-values at dynamic strain rates compares very well with the quasistatic data, indicating that there is no significant strain rate dependency of the r-values, at least within the rate regime investigated. The T3 and W51 essentially have the same r-values along TD, whereas the T711 and T721 are higher. Unlike the RD case, the TD r-value data suggests that although the magnitude of the r-values varies with the temper, their evolution with strain is less sensitive to the heat treatment.

The r-values for the ND samples show a wide range of scatter, with the overaged T721 having r-values closer to 1, followed by the slightly overaged T711 (Figure 6c). The high strain rate data, in general, falls in line with the quasistatic and thus the in agreement with the conclusion that the r-values are essentially rate independent. It is worth mentioning that in the previous study it was found that the ND r-values were highly sensitive to the initial texture of the material. It is important to recall that there are slight differences in the volume fraction of individual texture components (Table 1) and the effect of this is revealed by the simulation results, as discussed later. The experimental data reveals that the T3, W51 and T6 have r-values which are lower than the overaged T711 and T721 conditions.

The r-values for the 45 specimens are all greater than 1 and vary between ~1.4 to ~ 2, depending on the heat treatment (Figure 6d). The T3 material shows the largest r-values among all the tempers investigated; ~ 2 at low strains, which gradually decrease to 1.7 after 30% plastic strain. The W51 shows a constant r-value of ~1.6 throughout straining. For the peakaged (T6) specimen, the r-values are ~1.55 and exhibits some scatter with essentially remaining constant with straining. For the two overaged tempers investigated, T711 and T721, the r-values show rapid evolution like in case of RD, where they start from ~ 1.75 and rapidly decrease. The T711 seems to show a trend similar to T6, saturating at higher strain levels. The T721 tends to monotonically decrease to ~1.4. The dynamic r-values exhibit a similar trend, with a slightly larger scatter. Thus, along all the directions, the r-values tend toward 1 with aging, indicating that the material becomes more isotropic. The modeling which follows provides an explanation for why this is the case.

In the following section, the modified EPSC model, which takes into account the kinematic hardening due to an elastic inclusion, is applied along with the original EPSC model, to parse the effect of the initial texture and the precipitate induced effects, especially on the plastic strain anisotropy.

4.3 Modeling

In order to evaluate the capabilities of the EPSC model, for a case where the volume fraction of non-shearable precipitates should be minimal, the W51 material was chosen. It is admitted that a small volume fraction of shearable precipitates are undeniably present (given the large increase in strength over the freshly solutionized T3 case) and their effect is primarily accounted for via the initial critical resolved shear strength. The TD flow curves were used to *fit* the initial CRSS and Voce hardening parameters, and then the same parameter set is used to *predict* the flow curves and r-values of the RD, ND and 45 directions (Figure 7 a and b). The results show

that the model is able to successfully *predict* the yield as well as the strain hardening behavior along RD. For the 45 direction, although the model captures the initial yield strength, it underestimates the hardening behavior, resulting in a slightly lower flow stress overall. In case of ND, the model under-predicts the yield strength as well as fails to capture the rapid strain hardening, resulting in an underestimation of the flow stress by ~ 50 MPa. Problems with modeling the ND have abounded in this study of AA 7085, and through thickness variations in the texture are one known culprit.

Table 3: Voce hardening parameters for {111}<110> slip mode for W51 and T721

	τ_0	τ_1	θ_0
W51 - TD			
No particles (original EPSC)	195	80	250
T721 - TD			
No particles (original EPSC)	172	60	250
0.05 vol. fraction, no saturation	161	5	61
0.05 vol. fraction, saturation at 2% strain	161	50	170

Similar to the W51 case, the TD flow curves of T721 were fitted to obtain the Voce parameters (Table 3) and then the RD, ND and 45 responses were predicted and compared with the experimental data (Figures 8a and b). The simulation results of the original EPSC model show that the predicted flow curves for all the other directions are now underestimated, albeit to different extents; it is least under-predicted along RD and most along ND. Notably, the model fails to capture the initial rapid strain hardening along the RD. By incorporating a precipitate volume fraction of 0.05, the predictions are qualitatively improved; the hardening rate increases and the flow stresses shift in the right direction. In all cases, it predicts a lower flow stress anisotropy, which is in accordance with the experiments. By incorporating saturation of the backstress, the hardening behavior becomes more parabolic. After the initial rapid rise, the hardening rate

decreases in a manner that is similar to that observed experimentally. This is a direct result of enforcing exponential decay of the strain concentration, which reduces the strong polarization of the stresses.

As far as the strain anisotropy is concerned (Figure 6), the Schmid-Bonfoh model (Bonfoh et al., 2003; Schmitt et al., 1997) does capture the increase in r-value along RD and the decrease along the 45 direction with aging, by accounting for the presence of elastic precipitates. For these two directions, the r-values tend towards 1 with aging and this effect is clearly captured. The 'no ppt' simulation results match well with the T3/W51 data confirming that the material is more anisotropic when the non-shearable particles are absent.

As mentioned earlier, the r-values along ND were found to be highly sensitive to the initial texture, hence simulation results obtained with two initial textures (W51 and T721) are shown in Fig. 6c. Once the initial texture is accounted for, the simulated trends match that observed experimentally; for the W51 case the simulation results are close to the experimental data, irrespective of whether particles are accounted for or not, but for the T721 case, only by incorporating the particles does one obtain good agreement with the observed r-values. Along the TD, however, the results seem quite insensitive to the initial texture (Fig. 6b). The anisotropy along the TD is underestimated. The predictions are close to 1, whereas the measured values range from ~ 0.5-0.8.

5 Discussion

The temper dependence of strength and strain anisotropy of AA 7085 has been investigated. The experimental data reveal a systematic variation in the anisotropy of the flow strength, strain hardening, and particularly, plastic strain evolution for different heat treatment conditions. The general trends are clear. The peak-aged condition is characterized by flow curves

that show abrupt yield, the highest strength anisotropy, and the lowest strain hardening rates. In the solutionized state, the yield behavior is more gradual, the strength and strain anisotropy is lowest, and the strain hardening capacity is the highest. All other aging conditions lie intermediate to these two extremes. The 45 specimens are softest in all cases, except T6 where they show similar behavior as the ND. It is interesting to note that, starting from the solutionized condition, the flow strength anisotropy increases up to the T6 condition, after which it decreases again in the overaged condition. Perhaps, this is due to the transition from a shearable to non-shearable precipitate dominated response which affect the slip system selection, as discussed later.

It has also been shown that the sensitivity of the r-values to the initial texture is different along the various directions; the ND being most sensitive. This may explain the wide scatter in the r-values observed previously (Reyes et al., 2006). The r-values for RD, TD and 45 tend towards 1 with aging, i.e. the presence of the second phase particles increases the strength as well as modifies the strain anisotropy of the material. RD, TD and 45 all show consistent trends, whereas the ND results suggest that the r-values actually decrease when particle effects are considered. Another noteworthy point is that the r-values, particularly for the overaged condition show rapid evolution with strain, which is not observed in single phase alloys, where they remain almost constant throughout straining, at least for small strain levels, where texture evolution is minimal. This effect is well captured by the simulations, especially for the RD and 45 cases, only when the precipitate contribution is considered. Another point worth noting is that for non-overaged conditions, especially the T6 condition, the microstructure contains different metastable precipitate phases each of which resists shearing by the dislocations to varying degrees. Once over-aged, the precipitates are non-shearable at least up to a few percent strains (Moan and Embury, 1979), and hence, the effects of the internal stress become more apparent in the over-aged condition. Indeed,

the internal stresses of interest are those that develop because there are particles which remain elastic, despite being embedded in a plastic medium.

This empirical result helps to explain previous observation that conventional crystal plasticity modeling (with the viscoplastic self-consistent code known as VPSC), though it accounts for the initial texture, over-estimates the strain anisotropy. Those prior predictions better describe the strain anisotropy in the T3 and W51 tempers, whereas the T6, T711 and T721 tempered materials have an increasing population of shearable and non-shearable precipitates. The key feature which determines the anisotropy is slip system selection. The degree to which the precipitates alter the slip system selection, determines the changes in the observed strain anisotropy. There are two ways we can imagine this to occur. For shearable precipitates, a planar slip behavior is typically observed because, once a slip system is activated, it may actually undergo softening due to the shearing of the precipitates, and thus continue to remain active. In this case,, the grains tend to activate fewer slip systems. For non-shearable precipitates, backstresses may develop with straining which quickly "shut down" the initially active slip systems and force the grains to adopt other initially latent slip systems, which alters the way internal strains are distributed amongst the grains, and leads to a rapid evolution of the strain anisotropy within few percent strain (e.g., RD r-values for T721 temper, Fig. 6a). As a final caveat, the commercially heat treated tempers W51, T711 and T721 undergo a stretch in order to relieve macroscopic residual stresses. However, this stretch can also introduce dislocation based intragranular backstresses which can also alter the slip system selection (Zecevic and Knezevic, 2015). For the purpose of this study, only the effect of non-shearable precipitates on the slip system selection is considered and it is fully acknowledged that other effects also contribute to the overall response of the polycrystalline aggregate. Outstanding disagreement between the model and experiment

suggest that the effects of dislocation-based intragranular backstresses, recently treated by Zecevic et al. (2015), must also be considered along with the precipitate induced effects.

The conventional EPSC (no particle) simulation results for the W51 material describe the flow curves quite well, except along the ND. Similarly, the r-values for all directions examined are relatively well described, save along the TD. This suggests that the anisotropic behavior of this temper is mainly due to the crystallographic texture present in the material. On the other hand, for T721 material, the flow curve along RD is relatively well predicted, but the r-values are underestimated (see 'no ppt' simulations). This suggests that something other than the texture is influencing the strain anisotropy. Once a small volume fraction of precipitates/particles are introduced, via the Schmid-Bonfoh model (Bonfoh et al., 2003; Schmitt et al., 1997), the predictions shift in the correct direction. The new model captures the observed changes in both the flow strength and plastic strain anisotropy for all the directions except TD, where the results are unchanged by the inclusion of elastic particles. Thus, the precipitate-induced backstress provides a good explanation for the reduction in anisotropy observed to occur upon aging. Furthermore, if one observes the Voce parameters for T721 (Table 3), it can be seen that if no relaxation is considered; almost the whole contribution to strain hardening comes from the particle induced stresses. While it might be true for first few percent strain, at higher (>5%) strain levels, it seems somewhat unrealistic, since increases in the dislocation density also produces strain hardening. Furthermore, as mentioned earlier, incorporating relaxation of the backstress results in a decreasing hardening rate, similar to what is observed experimentally. When compared to the simulation results without saturation, not only does the '2% saturation' simulation results match the experimental data better, it is also considered to be closer to reality.

6 Conclusions

The strength and strain anisotropy of a precipitation hardenable aluminum alloy, 7085, in various tempers were measured experimentally, and the connections between the mechanical property observations and precipitate-induced backstress were explored using a modified EPSC modeling approach. The key points are:

1. AA 7085 is a new aerospace structural alloy, and hot-rolled plates exhibit a typical hot rolling texture consisting of strong brass and S components with milder recrystallization components (cube and Goss), which only vary in strength slightly from one temper to another (T3, T6, W51, T711, and T721).
2. The strain anisotropy (as characterized by r-values along RD, TD & 45° to RD) tend toward isotropy with increasing levels of aging. The anisotropy observations are essentially the same at quasistatic and dynamic (~1000 s^{-1}) strain rates, which greatly simplifies the characterization of the effect.
3. The strain rate sensitivity was found to be low and positive for all the tempers investigated, except T3, which exhibited a slightly negative rate sensitivity. It is hypothesized that the high solute content in the matrix interacts with dislocations to produce a dynamic strain ageing effect, in that case.
4. All the tempers, when compared to quasistatic loading, exhibit lower strain hardening rates under dynamic rates.
5. The original EPSC model can predict much of the anisotropy exhibited by the solutionized and water quenched (W51 & T3) materials, which do not contain non-shearable precipitates. For overaged (T711 & T721) material, the traditional EPSC model overpredicts the anisotropy, both of the flow stress and r-values.

6. Some of the changes in anisotropy from one sample type and another are shown to be due to the aforementioned subtle changes in the texture between samples sets. This is especially true for the case of samples compressed along the plate normal direction.
7. A micromechanical model has been incorporated in the EPSC framework and using this model, it is shown that incorporating a small volume fraction (0.05) of elastic second phase particles, the trend toward isotropy exhibited by aged material is reproduced.
8. When the backstresses are allowed to continue to build up without plastic relaxation, unrealistic levels of strain hardening are predicted. By incorporating an exponential decay in the backstress, the observed trends in anisotropy are retained, without over predicting the strain hardening.

Acknowledgements

The authors would like to thank ALCOA for providing the AA7085 plates, in W51, T711 and T721 tempers, used in this study. The authors would like to thank Frederic Barlat and Shi-Hoon Choi for suggesting us to look into this topic in detail. The research was sponsored by the United States Army Research Office under contract number W911NF-12-1-0455 monitored by Drs. Suveen Mathaudhu and David Stepp. The views and conclusions contained in this document are those of the authors and should not be interpreted as representing the official policies, either expressed or implied, of the Army Research Laboratory or the U.S. Government. The U.S. government is authorized to reproduce and distribute reprints for government purposes notwithstanding any copyright notation hereon.

APPENDIX

Stress and strain concentration tensors

In standard micromechanical formulation (Mura, 1982; Nemat-Nasser and Hori, 2013; Qu and Cherkaoui, 2006) one can define stress and strain concentration tensors which relate the properties of an individual grain to that of the effective medium.

Thus, for the case of a heterogeneous grain containing an elastic inclusion, embedded in an elastoplastic matrix, the stress concentration tensor, $\boldsymbol{B}$, can be defined in a manner which relates the stress increment of the precipitate and the matrix to the stress increment of the grain (Bonfoh et al., 2003; Schmitt et al., 1997):

$$d\sigma_{ij}^{ppt} = B_{ijkl}^{ppt} d\sigma_{kl}^{c} \text{ and } d\sigma_{ij}^{m} = B_{ijkl}^{m} d\sigma_{kl}^{c} \quad \text{(A1)}$$

Similarly, strain concentration tensors, $\boldsymbol{T}$, can also be defined which relate the strain increment of the precipitate and the matrix to the strain increment of the grain:

$$d\varepsilon_{ij}^{ppt} = T_{ijkl}^{ppt} d\varepsilon_{kl}^{c} \text{ and } d\varepsilon_{ij}^{m} = T_{ijkl}^{m} d\varepsilon_{kl}^{c} \quad \text{(A2)}$$

The strain concentration tensor for the particle, $\boldsymbol{T}^{ppt}$, obtained using a self-consistent approximation (Hill, 1965; Bonfoh et al., 2003; Qu and Cherkaoui, 2006) is given as :

$$T_{ijop}^{ppt} = \left(I_{ijop} + S_{ijkl}^{ppt} {L_{klmn}^{c}}^{-1} (C_{mnop}^{ppt} - L_{mnop}^{c})\right)^{-1} \quad \text{(A3)}$$

which can be expressed in a more symmetric form:

$$T_{pqmn}^{ppt} = \left(C_{mnop}^{ppt} + L_{ijkl}^{c} {S_{klmn}^{ppt}}^{-1} - L_{ijkl}^{c}\right)^{-1} \left(L_{ijkl}^{c} - L_{ijkl}^{c} {S_{klmn}^{ppt}}^{-1} + L_{ijkl}^{c}\right) \quad \text{(A4)}$$

$$T_{pqmn}^{ppt} = \left(C_{ijmn}^{ppt} + L_{ijkl}^{c} \left({S_{klmn}^{ppt}}^{-1} - I_{klmn}\right)\right)^{-1} \left(L_{mnop}^{c} + L_{ijkl}^{c} \left({S_{klmn}^{ppt}}^{-1} - I_{klmn}\right)\right) \quad \text{(A5)}$$

Denoting

$$L_{ijkl}^{c} \left({S_{klmn}^{ppt}}^{-1} - I_{klmn}\right) = L_{ijmn}^{*ppt} \quad \text{(A6)}$$

the strain concentration tensor can be written as:

$$T_{ijkl}^{ppt} = \left(C_{ijop}^{ppt} + L_{ijop}^{*}\right)^{-1}\left(L_{opkl}^{c} + L_{opkl}^{*}\right) \quad \text{(A7)}$$

Relationship between the stress and strain concentration tensors

Eqs. (A1) and (A2) can be substituted in the constitutive equation for an elastic particle, $d\sigma_{ij}^{ppt} = C_{ijkl}^{ppt} d\varepsilon_{kl}^{ppt}$ to get:

$$B_{ijop}^{ppt} d\sigma_{op}^{c} = C_{ijuv}^{ppt} T_{uvkl}^{ppt}\, d\varepsilon_{kl}^{c} \quad \text{(A8)}$$

Using the constitutive relation for the heterogeneous grain, $d\sigma_{ij}^{c} = L_{ijkl}^{c} d\varepsilon_{kl}^{c}$, Eq. (A8) becomes:

$$B_{ijop}^{ppt} L_{opkl}^{c} d\varepsilon_{kl}^{c} = C_{ijuv}^{ppt} T_{uvkl}^{ppt}\, d\varepsilon_{kl}^{c} \quad \text{(A9)}$$

from which the relation between the stress and strain concentration tensor is obtained as:

$$B_{ijop}^{ppt} = C_{ijuv}^{ppt} T_{uvmn}^{ppt} \left(L_{mnop}^{c}\right)^{-1} \quad \text{(A10)}$$

Derivation of the consistency condition (Eq. 16)

The total stress increment in the heterogeneous grain, $\boldsymbol{d\sigma}^{c}$, can be written using the rule of mixtures (Eq.10). Using Eq. (A1), the relationship between B_{ijkl}^{m} and B_{ijkl}^{ppt} can be obtained as:

$$B_{ijkl}^{m} = \left(I_{ijkl} - f B_{ijkl}^{ppt}\right)/(1-f) \quad \text{(A11)}$$

Thus, the consistency condition, Eq. (15) becomes,

$$m_{pq}^{\alpha}\left[d\sigma_{pq}^{c} + P_{pqmn}^{c}\left(C_{mnij}^{m}{}^{-1}\frac{\left(I_{ijkl} - f B_{ijkl}^{ppt}\right)}{(1-f)} d\sigma_{kl}^{c} + \sum_{\alpha} m_{mn}^{\alpha}\, d\gamma^{\alpha}\right)\right] = \sum_{\beta} V^{\alpha}(\Gamma) h^{\alpha\beta}\, d\gamma^{\beta} \quad \text{(A12)}$$

Using $d\varepsilon_{ij}^{c,pl} = (1-f)\sum_{\alpha} m_{ij}^{\alpha}\, d\gamma^{\alpha} = \sum_{\alpha} m_{ij}^{\alpha}\, d\gamma^{\alpha,c}$ where, $d\gamma^{\alpha,c} = (1-f) d\gamma^{\alpha}$ and rearranging, one obtains:

$$\boldsymbol{m_{ij}^{\alpha}}\left[(\mathbf{1}-\boldsymbol{f})\boldsymbol{I_{ijuv}} + \boldsymbol{P_{ijkl}^{c}}\,\boldsymbol{C_{klmn}^{m}}^{-1}\left(\boldsymbol{I_{mnuv}} - \boldsymbol{f B_{mnuv}^{ppt}}\right)\right]\boldsymbol{d\sigma_{uv}^{\alpha}} = \sum_{\boldsymbol{\beta}}\left(\boldsymbol{V^{\alpha}(\Gamma) h^{\alpha\beta}} - \boldsymbol{m_{ij}^{\alpha}\, P_{ijkl}^{c}\, m_{kl}^{\alpha}}\right)\boldsymbol{d\gamma^{\beta,c}} \quad \text{(A13)}$$

Substituting $B_{ijop}^{ppt} = C_{ijuv}^{ppt} T_{uvmn}^{ppt}\left(L_{mnop}^{c}\right)^{-1}$ in Eq. (A13) leads to the final expression for consistency condition, Eq. (16).

Polarization tensor ($\boldsymbol{P^c}$) in terms of the strain concentration tensor ($\boldsymbol{T^{ppt}}$)

Using the constitutive relationship and the stress concentration tensor for the matrix one obtains (Bonfoh et al., 2003) :

$$d\sigma_{kl}^{m} = d\sigma_{ij}^{c} + \left(I_{ijkl} - \left(B_{ijkl}^{m}\right)^{-1}\right) L_{klmn}^{m} d\varepsilon_{mn}^{m} \tag{A14}$$

which on comparing with Eq.(14), yields the expression for $\boldsymbol{P^c}$ as:

$$P_{ijmn}^{c} = \left(I_{ijkl} - \left(B_{ijkl}^{m}\right)^{-1}\right) L_{klmn}^{m} = L_{klop}^{m} - \left({L_{klmn}^{m}}^{-1} B_{mnop}^{m}\right)^{-1} \tag{A15}$$

To eliminate the terms containing matrix properties, using Eq. (8):

$$\left(L_{ijkl}^{c}\right)^{-1} d\sigma_{kl}^{c} = f\left(C_{ijkl}^{ppt}\right)^{-1} d\sigma_{kl}^{ppt} + (1-f)\left(L_{ijkl}^{m}\right)^{-1} d\sigma_{kl}^{m} \tag{A16}$$

and substituting Eq. (A1) in it leads to:

$$\left(L_{ijkl}^{c}\right)^{-1} = f\left(C_{ijmn}^{ppt}\right)^{-1} B_{mnkl}^{ppt} + (1-f)\left(L_{ijmn}^{m}\right)^{-1} B_{mnkl}^{m}$$

From which expressions of L_{klmn}^{m} and $\left(B_{ijkl}^{m}\right)^{-1}$ can be substituted into Eq. (A15) to obtain $\boldsymbol{P^c}$ as:

$$P_{ijop}^{c} = f\left(I_{ijuv} - B_{ijuv}^{ppt}\right)\left(\left(L_{uvop}^{c}\right)^{-1} - f\left(C_{uvmn}^{ppt}\right)^{-1} B_{mnop}^{ppt}\right)^{-1} \tag{A17}$$

To eliminate the grain compliance, substituting the relationship Eq. (A7) in the expression for $\boldsymbol{P^c}$, Eq. (A17) and simplifying one obtains:

$$P_{ijop}^{c} = f\left(I_{ijop} - C_{ijuv}^{ppt} T_{uvmn}^{ppt}\left(L_{mnqr}^{c}\right)^{-1}\right)\left(\left(L_{qruv}^{c}\right)^{-1}\left(I_{uvop} - f\,T_{uvop}^{ppt}\right)\right)^{-1} \tag{A18}$$

Using standard rules of matrix inversion and commutative properties of double contraction, this simplifies to:

$$P_{ijop}^{c} = f\left(L_{ijop}^{c} - C_{ijuv}^{ppt} T_{uvmn}^{ppt}\right)\left(I_{mnop} - f T_{mnop}^{ppt}\right)^{-1} \tag{A20}$$

References

Agnew, S.R., Whittington, W.R., Oppedal, A., El Kadiri, H., Shaeffer, M., Ramesh, K.T., Bhattacharyya, J.J., Delorme, R., Davis, B., 2014. Dynamic Behavior of a Rare-Earth-Containing Mg Alloy, WE43B-T5, Plate with Comparison to Conventional Alloy, AM30-F. Jom 66, 277–290. doi:10.1007/s11837-013-0830-x

Anjabin, N., Karimi Taheri, A., Kim, H.S., 2014. Crystal plasticity modeling of the effect of precipitate states on the work hardening and plastic anisotropy in an Al-Mg-Si alloy. Comput. Mater. Sci. 83, 78–85. doi:10.1016/j.commatsci.2013.09.031

Ashby, M., 1970. The deformation of plastically non-homogeneous materials. Philos. Mag. 21, 399–424. doi:10.1007/s13398-014-0173-7.2

Atkinson, J.., Brown, L.., Stobbs, W.M., 1974. The work-hardening of copper-silica IV. The Bauschinger effect and plastic relaxation. Philos. Mag. 30, 1247–1280.

Barlat, F., Liu, J., 1998. Precipitate-induced anisotropy in binary Al-Cu alloys. Mater. Sci. Eng. A 257, 47–61. doi:10.1016/S0921-5093(98)00823-5

Bate, P., Roberts, W.T., Wilson, D., 1982. The plastic anisotropy of two-phase aluminium alloys - II Anisotropic behavior in load reversal tests. Acta Metall. 30, 725–737.

Bate, P., Roberts, W.T., Wilson, D. V, 1981. The plastic anisotropy of two-phase aluminum alloys -- I. Anisotropy in unidirectional deformation. Acta Metall. 29, 1797–1814.

Bhattacharyya, J.J., Agnew, S.R., Lee, M.M., Whittington, W.R., El Kadiri, H., 2017. Measuring and modeling the anisotropic, high strain rate deformation of Al alloy, 7085, plate in T711 temper. Int. J. Plast. 93, 46–63.

Bhattacharyya, J.J., Wang, F., Wu, P.D., Whittington, W.R., El Kadiri, H., Agnew, S.R., 2016. Demonstration of alloying, thermal activation, and latent hardening effects on quasi-static and dynamic polycrystal plasticity of Mg alloy, WE43-T5, plate. Int. J. Plast. 81, 123–151. doi:10.1016/j.ijplas.2016.01.005

Bonfoh, N., Carmasol, A., Lipinski, P., 2003. Modeling of intra-crystalline hardening of materials with particles. Int. J. Plast. 19, 1167–1193. doi:10.1016/S0749-6419(02)00015-3

Brown, L.., Clarke, D.., 1975. Work hardening due to internal stresses in composite materials. Acta Metall. 23, 821–830.

Brown, L.M., Stobbs, W.M., 1976. The work-hardening of copper-silica V. equlibrium plastic relaxation by secondary dislocations. Philos. Mag. 34, 351–372. doi:10.1007/s13398-014-0173-7.2

Brown, L.M., Stobbs, W.M., 1971. The work hardening of copper-silica I. A model based on internal stresses, with no plastic relaxation. Philos. Mag. 23, 1185–1199.

Brown, L.M., Stobbs, W.M., 1971. The work-hardening of copper-silica II. The role of plastic relaxation. Philos. Mag. 23, 1201–1233. doi:10.1007/s13398-014-0173-7.2

Busso, E.P., Meissonnier, F.T., O'Dowd, N.P., 2000. Gradient-dependent deformation of two-phase single crystals. J. Mech. Phys. Solids 48, 2333–2361. doi:10.1016/S0022-5096(00)00006-5

Caceres, C.., Griffiths, J.R., Reiner, P., 1996. The influence of microstructure on the Bauschinger effect in an Al-Si-Mg casting alloy. Acta Metall. 44, 14–23.

Chen, W.W., Song, B., 2010. Split Hopkinson (Kolsky) bar: design, testing and applications. Springer Science & Business Media.

Cheng, L.M., Poole, W.J., Embury, J.D., Lloyd, D.J., 2003. The influence of precipitation on the work-hardening behavior of the aluminum alloys AA6111 and AA7030. Metall. Mater. Trans. A 34, 2473–2481. doi:10.1007/s11661-003-0007-2

Choi, S.H., Barlat, F., Liu, J., 2000a. Effect of Precipitates on Plastic Anisotropy of Polycrystalline Aluminum Alloys. Metall. Mater. Trans. A Phys. Metall. Mater. Sci. 32, 2239–2247. doi:10.4028/www.scientific.net/MSF.331-337.1327

Choi, S.H., Barlat, F., Liu, J., 2000b. Effect of Precipitates on Plastic Anisotropy of Polycrystalline Aluminum Alloys. Mater. Sci. Forum 331–337, 1327–1332. doi:10.4028/www.scientific.net/MSF.331-337.1327

Corbin, S.F., and Wilkinson, D.S., 1994. the Influence of Particle Distribution on the Mechanical Response of a Particulate Metal Matrix Composite. Acta Metall. 42, 1311–1318.
Deschamps, A., Bigot, A., Livet, F., Auger, P., Brechet, Y., Blavette, D., 2001. A Comparative Study of Precipitate Composition and Volume Fraction in an Al–Zn–Mg Alloy using Tomographic Atom Probe and Small-Angle X-ray Scattering. Philos. Mag. A 81, 2391–2414. doi:10.1080/01418610110038439
Doherty, K., Squillacioti, R., Cheeseman, B., Placzankis, B., Gallardy, D., 2012. Expanding the Availability of Lightweight Aluminum Alloy Armor Plate Procured From Detailed Military Specifications. ICAA13 13th Int. Conf. Alum. Alloy. 541–546.
Dumont, D., Deschamps, a., Bréchet, Y., Sigli, C., Ehrström, J.C., 2004. Characterisation of precipitation microstructures in aluminium alloys 7040 and 7050 and their relationship to mechanical behaviour. Mater. Sci. Technol. 20, 567–576. doi:10.1179/026708304225016662
Dumont, M., Lefebvre, W., Doisneau-Cottignies, B., Deschamps, A., 2005. Characterisation of the composition and volume fraction of η′ and η precipitates in an Al-Zn-Mg alloy by a combination of atom probe, small-angle X-ray scattering and transmission electron microscopy. Acta Mater. 53, 2881–2892. doi:10.1016/j.actamat.2005.03.004
Eshelby, J.D., 1957. The Determination of the Elastic Field of an Ellipsoidal Inclusion, and Related Problems. Proc. R. Soc. A Math. Phys. Eng. Sci. 241, 376–396. doi:10.1098/rspa.1957.0133
Estrin, Y., 1996. "Dislocation-density-related constitutive modeling.," in: Krausz, A.., Krausz, K. (Eds.), Unified Constitutive Laws of Plastic Deformation. Academic Press, Inc, pp. 82–84.
Follansbee, P.S., 2014. Fundamentals of Strength—Principles, Experiment, and Application of an Internal State Variable Constitutive Model. the Minerals. Met. Mater. Soc. John Wiley Sons, Inc., Hoboken.
Fribourg, G., Brechet, Y., Deschamps, A., Simar, A., 2011. Microstructure-based modelling of isotropic and kinematic strain hardening in a precipitation-hardened aluminium alloy. Acta Mater. 59, 3621–3635. doi:10.1016/j.actamat.2011.02.035
Gray, G.T.T., 2000. Classic Split-Hopkinson Pressure Bar Testing. Mater. Park. OH ASM Int. 2000. 462–476.
Han, C.S., Kim, J.H., Chung, K., Kang, T.J., 2006. Modeling the plastic deformation of crystals with thin precipitates. Int. J. Solids Struct. 43, 2398–2421. doi:10.1016/j.ijsolstr.2005.06.032
Han, C.S., Wagoner, R.H., Barlat, F., 2004. On precipitate induced hardening in crystal plasticity: theory. Int. J. Plast. 20, 477–494. doi:10.1016/j.ijplas.2003.11.002
Hielscher, R., Schaeben, H., 2008. A novel pole figure inversion method: Specification of the MTEX algorithm. J. Appl. Crystallogr. 41, 1024–1037. doi:10.1107/S0021889808030112
Hill, R., 1966. Generalized constitutive relations for incremental deformation of metal crystals by multislip. J. Mech. Phys. Solids 14, 95–102. doi:10.1016/0022-5096(66)90040-8
Hill, R., 1965. Continuum Micro-Mechanics of Elastoplastic polycystals. J. Mech. Phys. Solids 13, 89–101.
Hosford, W.F., Zeisloft, R.H., 1972. The anisotropy of age-hardened Al-4 Pct Cu single crystals during plane-strain compression. Metall. Trans. 3, 113–121.
Hutchinson, J.. ., 1970. Elastic-Plastic Behavior of Polycrystalline Metals and Composites. Proc. R. Soc. London A Math. Phys. Eng. Sci. 319, 247–272.
Jain, A., Agnew, S.R., 2007. Modeling the temperature dependent effect of twinning on the behavior of magnesium alloy AZ31B sheet. Mater. Sci. Eng. A 462, 29–36. doi:10.1016/j.msea.2006.03.160
Jobson, P., Roberts, W.T., 1977. Directionality in a precipitation-hardened alloy. Metall. Mater. Trans. A 8, 2013–2014.
Kubin, L.P., Estrin, Y., 1991. Dynamic strain ageing and the mechanical response of alloys. J. Phys. III 1, 929–943.
Moan, G.D., Embury, J.D., 1979. A study of the Bauschinger effect in Al-Cu alloys. Acta Metall. 27, 903–914.
Mulay, R.P., Clausen, B., Agnew, S.R., 2011. In-situ neutron diffraction study of the bauschinger effect in B2 structured CoZr. Metall. Mater. Trans. A Phys. Metall. Mater. Sci. 42, 60–70.

doi:10.1007/s11661-010-0389-x
Mura, T., 1982. Micromechanics of Defects in Solids,(1982). Martinus Nijhoff.
Neil, C.J., Wollmershauser, J.A., Clausen, B., Tomé, C.N., Agnew, S.R., 2010. Modeling lattice strain evolution at finite strains and experimental verification for copper and stainless steel using in situ neutron diffraction. Int. J. Plast. 26, 1772–1791. doi:10.1016/j.ijplas.2010.03.005
Nemat-Nasser, S., Hori, M., 2013. Micromechanics: overall properties of heterogeneous materials. Elsevier.
Park, J.K., Ardell, A.J., 1983. Microstructures of the commercial 7075 Al alloy in the T651 and T7 tempers. Metall. Trans. A 14, 1957–1965. doi:10.1007/BF02662363
Poole, W.J., Wang, X., Lloyd, D.J., Embury, J.D., 2007. The shearable – non-shearable transition in Al – Mg – Si – Cu precipitation hardening alloys : implications on the distribution of slip , work hardening and fracture. Philos. Mag. 37–41. doi:10.1080/14786430500154935
Proudhon, H., Poole, W.J., Wang, X., Bréchet, Y., 2008. The role of internal stresses on the plastic deformation of the Al–Mg–Si–Cu alloy AA6111. Philos. Mag. 88, 621–640. doi:10.1080/14786430801894569
Qu, J., Cherkaoui, M., 2006. Fundamentals of micromechanics of solids. John Wiley & Sons, Inc., Hoboken, NJ.
Reyes, A., Hopperstad, O.S., Lademo, O.-G., Langseth, M., 2006. Modeling of textured aluminum alloys used in a bumper system: Material tests and characterization. Comput. Mater. Sci. 37, 246–268. doi:10.1016/j.commatsci.2005.07.001
Russell, K.G., Ashby, M.F., 1970. Slip in aluminum crystals containing strong, plate-like particles. Acta Metall. 18, 891–901. doi:10.1016/0001-6160(70)90017-9
Schmitt, C., Lipinski, P., Berveiller, M., 1997. Micromechanical modelling of the elastoplastic behavior of polycrystals containing precipitates— Application to hypo- and hyper-eutectoid steels. Int. J. Plast. 13, 183–199. doi:10.1016/S0749-6419(95)00007-0
Sehitoglu, H., Foglesong, T., Maier, H.J., 2005. Precipitate effects on the mechanical behavior of aluminum copper alloys: Part II. Modeling. Metall. Mater. Trans. a-Physical Metall. Mater. Sci. 36A, 763–770.
Simar, A., Brechet, Y., de Meester, B., Denquin, A., Pardoen, T., 2007. Sequential modeling of local precipitation, strength and strain hardening in friction stir welds of an aluminum alloy 6005A-T6. Acta Mater. 55, 6133–6143. doi:10.1016/j.actamat.2007.07.012
Srivatsan, T.S., Sriram, S., Veeraraghavan, D., Vasudevan, V.K., 1997. Microstructure, tensile deformation and fracture behaviour of aluminium alloy 7055. J. Mater. Sci. 32, 2883–2894. doi:10.1023/A:1018676501368
Stoltz, R.E., Pelloux, R.M., 1976. The Bauschinger effect in precipitation strengthened aluminum alloys. Metall. Trans. A 7, 1295–1306.
Tome, C.N., Oliver, E.C., Wollmershauser, J.A., 2002. Code Elasto-Plastic Self-Consistent (EPSC). Los Alamos Natl. Lab. New Mex.
Turner, P.A., Tomé, C.N., 1994. A study of residual stresses in Zircaloy-2 with rod texture. Acta Metall. Mater. 42, 4143–4153. doi:10.1016/0956-7151(94)90191-0
Wilson, D.., 1965. Reversible work hardening in alloys of cubic metals. Acta Metall. 13, 807–814. doi:10.1016/0001-6160(65)90145-8
Withers, P.J., Stobbs, W.M., Pedersen, O.B., 1989. The Application of the Eshelby Method of Internal Stress Determination to Short Fiber Metal Matrix Composites. Acta Metall. 37, 3061–3084.
Yassar, R.S., Mesarovic, S.D., Field, D.P., 2007. Micromechanics of hardening of elastic-plastic crystals with elastic inclusions: I - Dilute concentration. Int. J. Plast. 23, 1901–1917. doi:10.1016/j.ijplas.2007.03.013
Zecevic, M., Knezevic, M., 2015. A dislocation density based elasto-plastic self-consistent model for the prediction of cyclic deformation: Application to AA6022-T4. Int. J. Plast. 72, 200–217. doi:10.1016/j.ijplas.2015.05.018

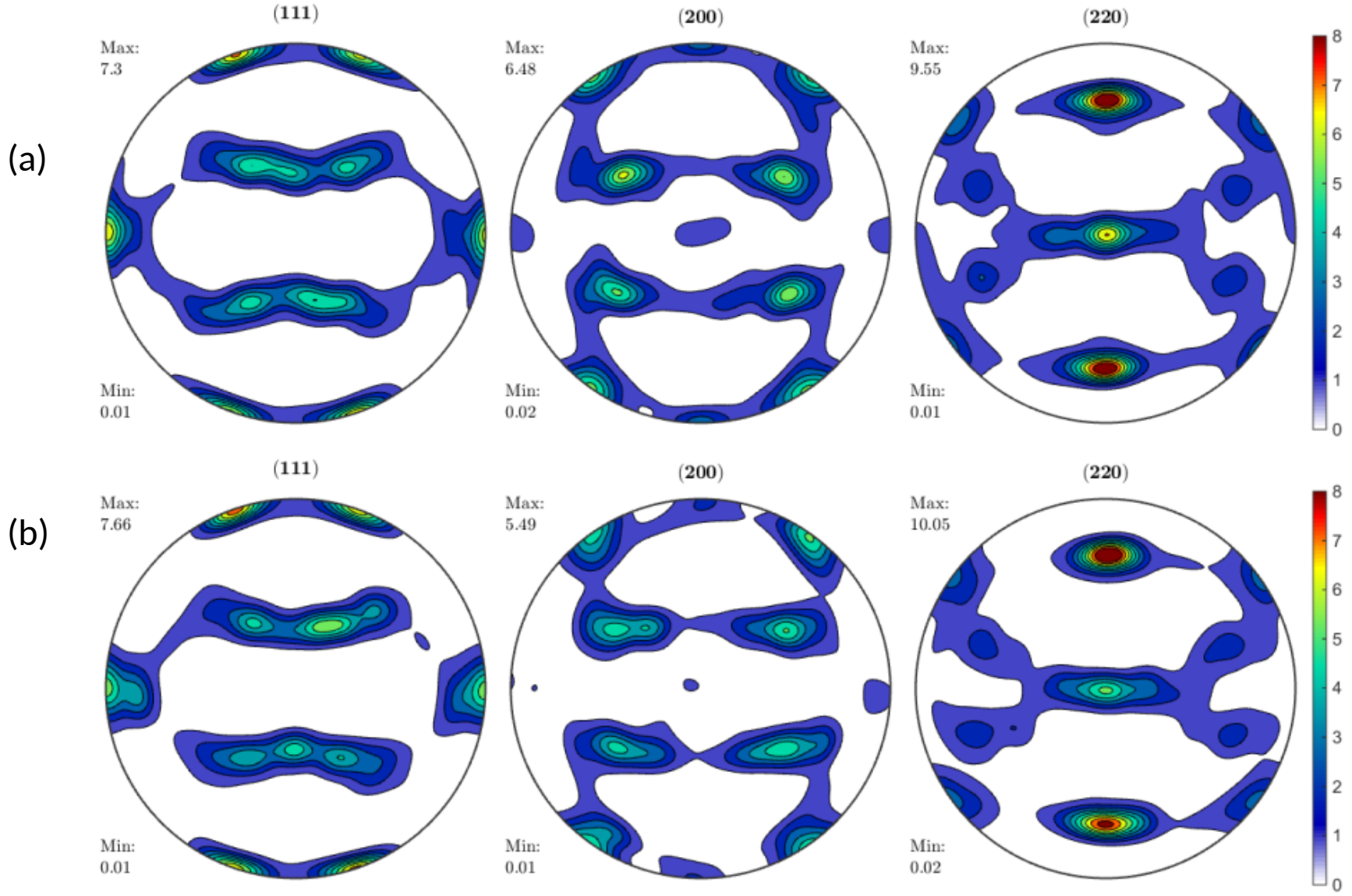

Figure 1: Textures measured at the plate mid-plane in the a) as-quenched temper (T3) and b) the over-aged condition known as T721.

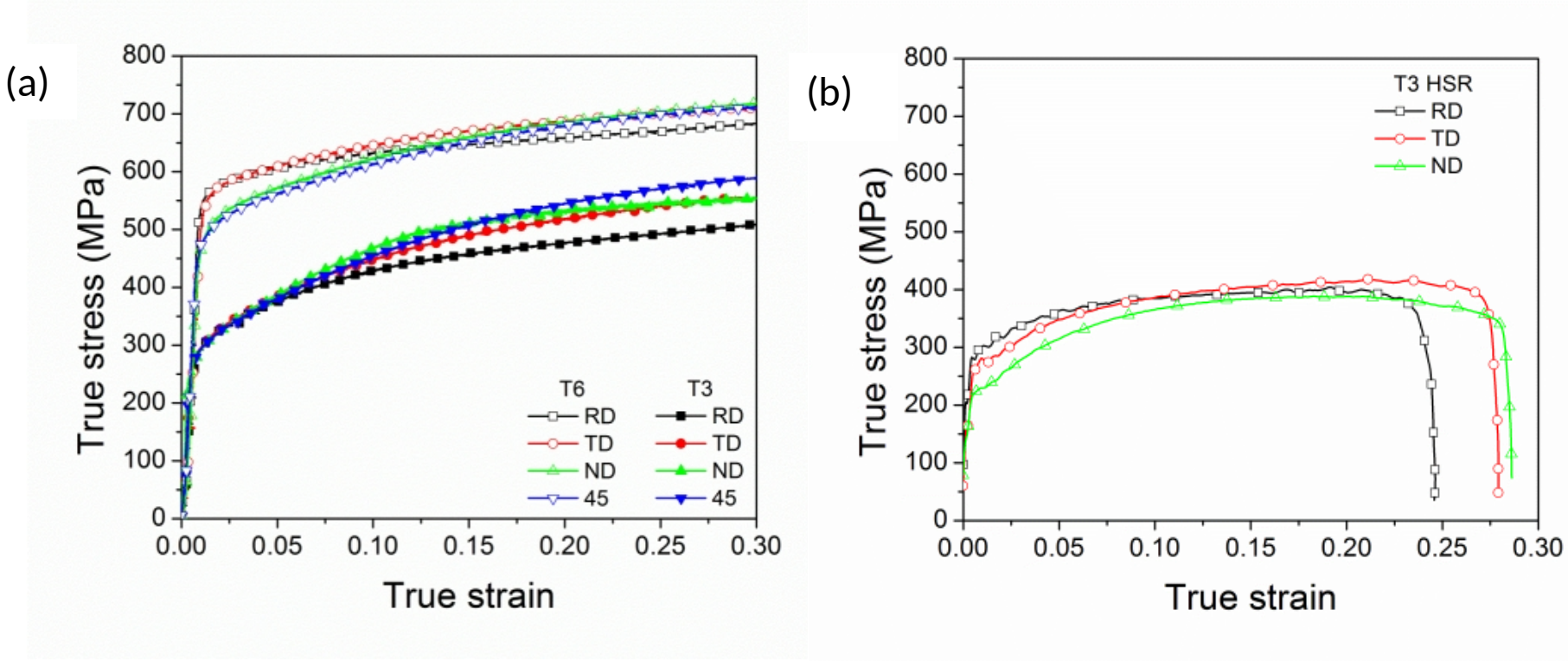

Figure 2: Experimental flow curves for a) T3 and T6 temper at 0.001 s^{-1} showing the dramatic age hardening response and b) T3 temper at ~1000 s^{-1}. It is interesting to note that the dynamic flow strength of T3 is lower at the higher rate.

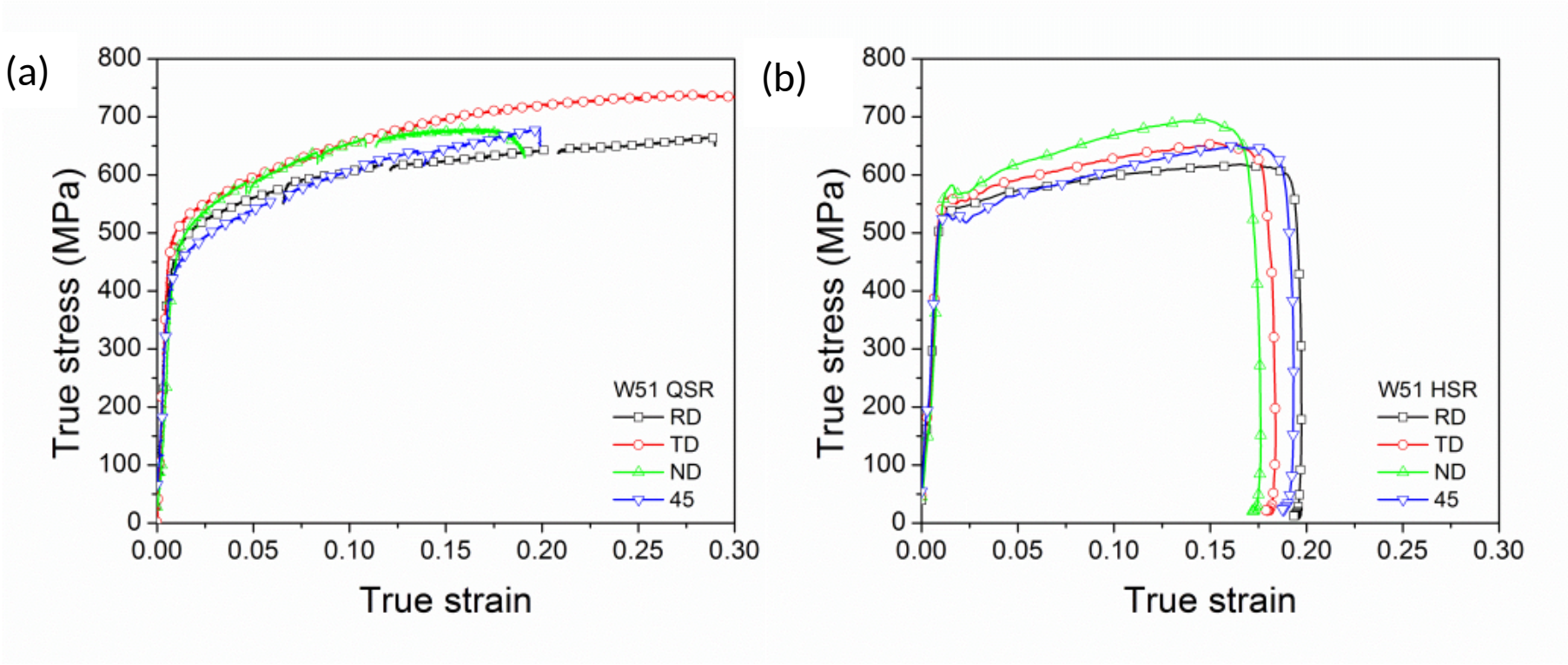

Figure 3: Experimental flow curves for W51 temper at a) 0.001 s^{-1} and b) ~1000 s^{-1}.

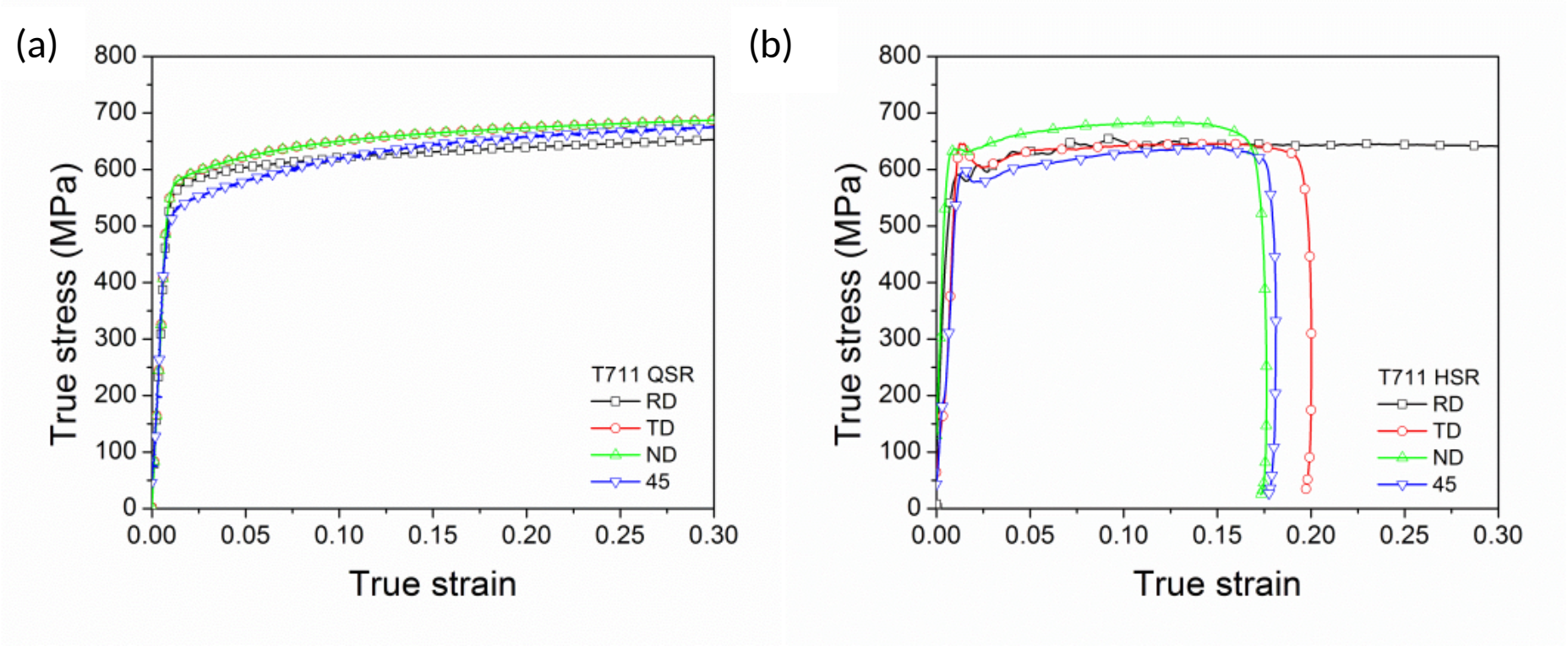

Figure 4: Experimental flow curves for T711 temper at a) 0.001 s^{-1} and b) ~ 1000 s^{-1}

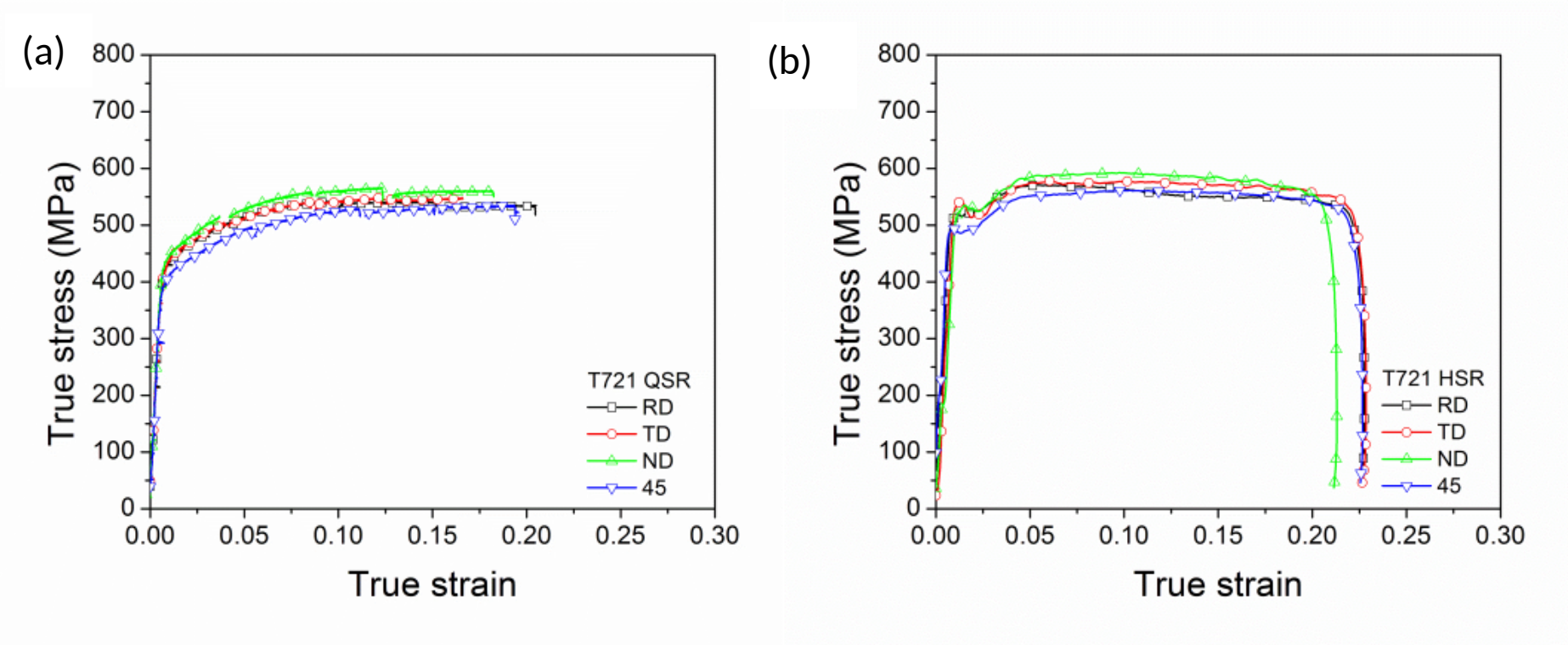

Figure 5: Experimental flow curves for T721 temper at a) 0.001 s^{-1} and b) ~1000 s^{-1}.

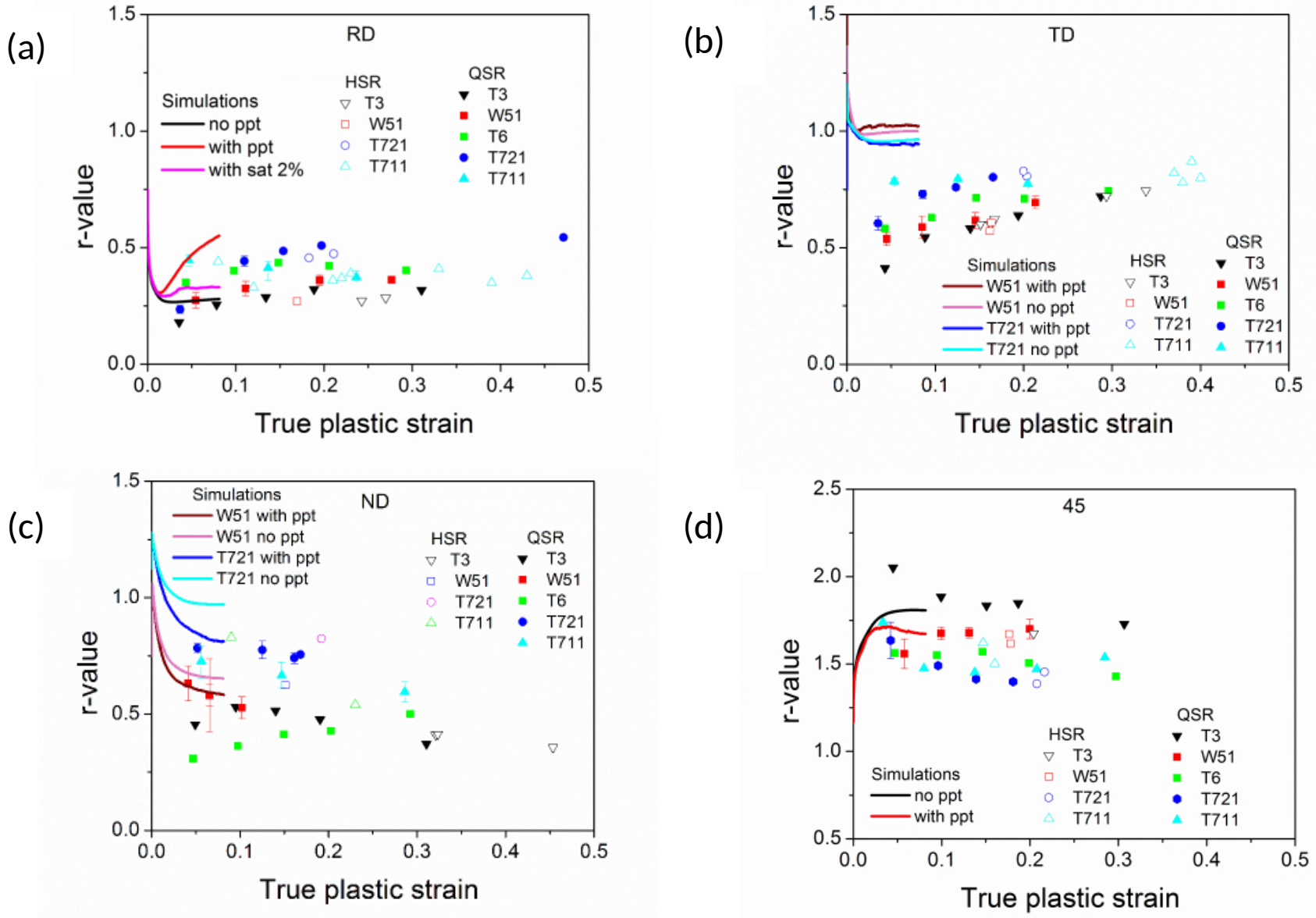

Figure 6: Experimental and simulated r-value evolution as a function of plastic strain, for T3, W51,T6, T711 and T721 temper, at both quasistatic and dynamic strain rates along a) RD b) TD c) ND and d) 45

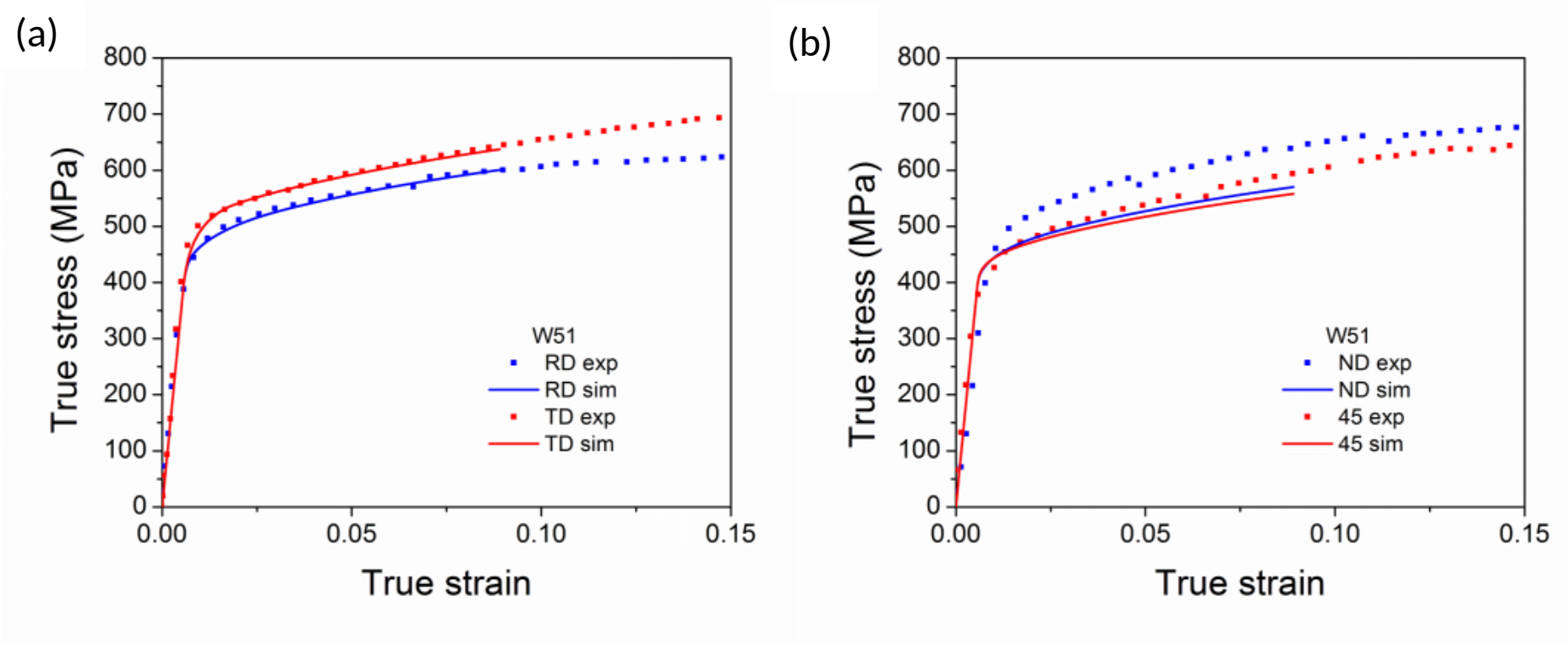

Figure 7: Experimental and simulated flow curves for W51 a) fitted along TD and predicted along RD b) predicted along ND and 45

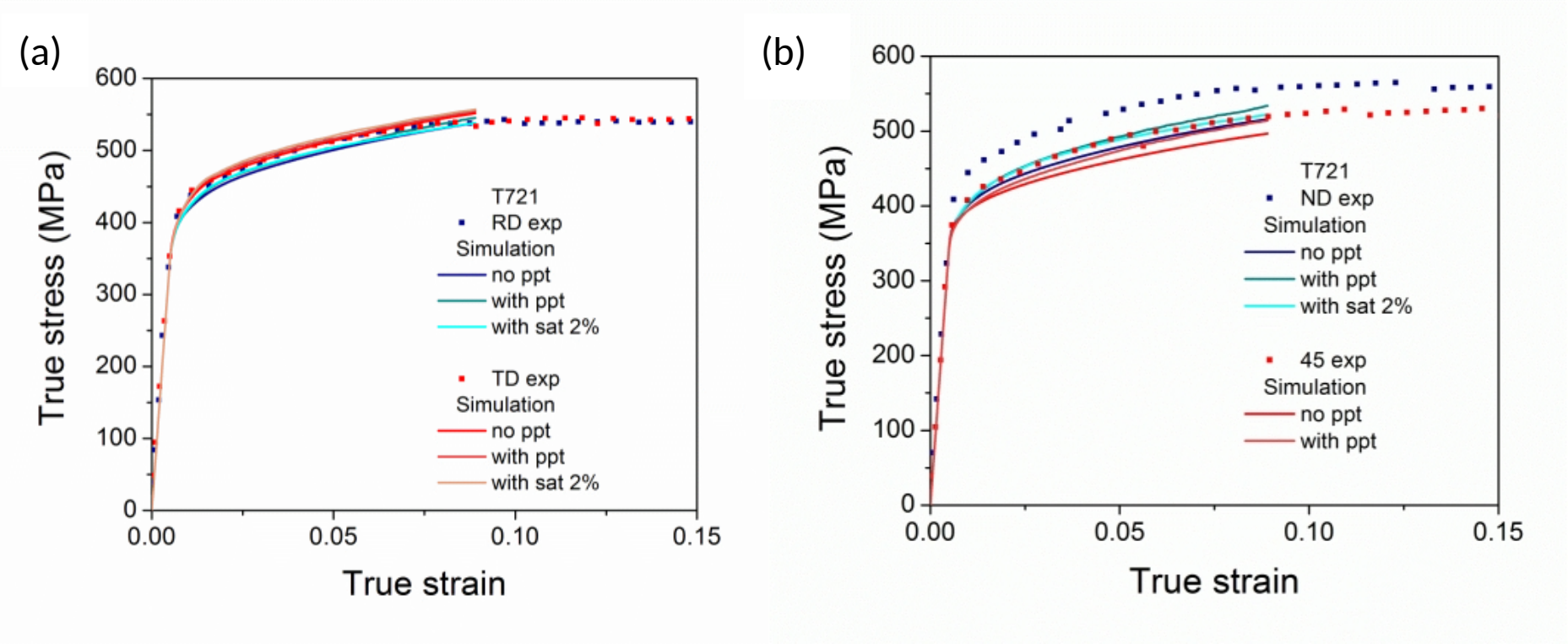

Figure 8: Experimental and simulated flow curves for T721a) fitted along TD and predicted along RD b) predicted along ND and 45. All modeling approaches fit equally well, since the parameters were independently adjusted for each case to obtain the best possible description of the experimental data.

Elsevier Editorial System(tm) for Acta Materialia

Manuscript Draft

Manuscript Number:

Title: Slip mode dependency of dislocation shearing and looping of precipitates in Mg alloy WE43

Article Type: Full length article

Keywords: shearable precipitates; order strengthening; anti-phase domain boundary; crystal plasticity; precipitation hardening.

Corresponding Author: Dr. Jishnu J Bhattacharyya,

Corresponding Author's Institution: University of Virginia

First Author: Jishnu J Bhattacharyya

Order of Authors: Jishnu J Bhattacharyya; Fulin Wang; Nicole Stanford; Sean R Agnew

Abstract: The effect of precipitates on the strength of Mg alloy,WE43, has been investigated. Transmission electron microscopy(TEM) provides unequivocal evidence that the ordered prismatic plate-shaped β' precipitates are sheared by basal slip of <a> dislocations. However, non-basal <a> and pyramidal <c+a> dislocations are unable to shear the precipitates, and instead bow around them during plastic deformation. In the latter case the Orowan looping model accurately predicts precipitate hardening. For the case of the shearable particles, it is proposed that order strengthening is the dominant mechanism by which the β' phase provides strengthening to the basal slip system, and a new model quantifying this effect is developed. Using this model in conjunction with TEM observations and elastoplastic self-consistent polycrystal modeling, the anti-phase boundary energy (APB) of the precipitates is estimated to be 210 mJ/m2. The present work has significant implications for Mg alloy design strategies, and emphasizes the importance of considering both precipitate shearing and Orowan looping of precipitates. Finally, it suggests the value of making first-principles predictions of APB energies (γ-surfaces) of the candidate strengthening phases.

Suggested Reviewers: Joseph Robson
Professor, School of Materials, Univeristy of Manchester
joseph.d.robson@manchester.ac.uk
Prof. Robson is an expert in the field of precipitation hardening in Mg based alloys.

Alok Singh
Chief Researcher, National Institute for Materials Science (NIMS)
alok.singh@nims.go.jp
Dr. Singh is an expert in TEM characterization and precipitation strengthening mechanisms in Mg alloys

Warren Poole
Professor, Department of Materials Engineering, University of British Columbia

warren.poole@ubc.ca
Prof. Poole is an expert in strength modeling and structure-property relationships in metallic alloys

Hahn Choo
Associate Professor, Materials Science and Engineering, University of Tennessee, Knoxville
hchoo@utk.edu
Prof. Choo is an expert in deformation behavior of non-cubic materials.

August 21, 2017

To the editor,

We hope that you and the reviewers find this work to be a significant addition to our current understanding of age-hardenable Mg alloys and hcp alloys, in general. It is an original piece of work that provides evidence of shearing of precipitates by basal <a> dislocations and how this phenomenon affects the flow behavior of the alloy. Furthermore, it emphasizes that for non-cubic materials where multiple slip modes are active, different modes can interact (loop vs shear) with the precipitates differently.

Sincerely,

Jishnu Bhattacharyya

Slip mode dependency of dislocation shearing and looping of precipitates in Mg alloy WE43

J.J. Bhattacharyya[1], F. Wang[1], N.Stanford[2], S. R. Agnew[1]

[1]Materials Science and Engineering, University of Virginia, Charlottesville, Virginia, U.S.A.

[2]Institute for Frontier Materials, Deakin University, Victoria 3216, Australia

ABSTRACT

The effect of precipitates on the strength of Mg alloy, WE43, has been investigated. Transmission electron microscopy (TEM) provides unequivocal evidence that the ordered prismatic plate-shaped β' precipitates are sheared by basal slip of <a> dislocations. However, non-basal <a> and pyramidal <c+a> dislocations are unable to shear the precipitates, and instead bow around them during plastic deformation. In the latter case the Orowan looping model accurately predicts precipitate hardening. For the case of the shearable particles, it is proposed that order strengthening is the dominant mechanism by which the β' phase provides strengthening to the basal slip system, and a new model quantifying this effect is developed. Using this model in conjunction with TEM observations and elastoplastic self-consistent polycrystal modeling, the anti-phase boundary energy (APB) of the precipitates is estimated to be 210 mJ/m^2. The present work has significant implications for Mg alloy design strategies, and emphasizes the importance of considering both precipitate shearing and Orowan looping of precipitates. Finally, it suggests the value of making first-principles predictions of APB energies (γ-surfaces) of the candidate strengthening phases.

Keywords: shearable precipitates, order strengthening, anti-phase domain boundary, crystal plasticity, precipitation hardening

1 INTRODUCTION

For over a decade, the design of precipitation strengthened Mg alloys has been built on the assumption that precipitates are non-shearable. Nie [1] provided initial guidance of this effort by demonstrating that prismatic plate shaped precipitates would be the most effective obstacles of basal slip, relative to spherical or c-axis rod-shaped precipitates of the same volume fraction and number density. Nie's initial efforts were supplemented by Robson et al. [2,3] who made calculations of the Orowan strengthening of prismatic slip by variously shaped precipitates and more recently by some of the present authors, who extended the analysis to include pyramidal slip of <a> and <c+a> dislocations [4]. Although these calculations provide useful estimates of the inter-particle spacings of variously shaped precipitates, it has recently been demonstrated that certain precipitates within Mg alloys are shearable [5] . Consequently, strength estimates based on the Orowan looping model cannot be applied. This observation has made it necessary to reconsider particle shearing, and for the case of magnesium alloys, particle shearing is an aspect of plastic deformation that has not yet been quantitatively assessed in the literature. Until we understand which aspects of particle shearing contribute the most to strengthening, it will not be possible to design precipitate strengthened alloys for maximum strength. Developing a deeper understanding of this phenomenon is therefore warranted.

In the present paper, the WE-family of Mg alloys (where the "W" stands for Y and "E" for Nd-rich mischmetal additions) is chosen for study because its precipitation [e.g., 6–9] and deformation characteristics are well known [10,11]. Polycrystal plasticity modeling has been shown to be a robust method to study Mg alloy deformation characteristics, and can be applied to precipitate strengthened alloys with different textures and grain sizes. The present paper utilizes this modeling approach to make accurate assessments of the precipitate strengthening of the

individual slip modes. This quantification is used in conjunction with transmission electron microscopy to develop a comprehensive description of the factors leading to precipitate strengthening of the rare-earth containing alloy WE43.

2 EXPERIMENTAL METHODS

2.1 Materials, heat treatment, and mechanical testing

This study is a follow-up on another study which explored various heat treatment strategies for WE43 [12]. The materials and heat treatments procedures are described there. Specifically, a 38 mm (1.5 inch) thick WE43-T5 plate, provided by Magnesium Elektron North America, was used. This as-received material was subjected to a solutionizing heat treatment (SHT) at 798 K (525 °C) for 8 hours and subsequently aged at 210 °C for 64 h, to produce the T6 temper. The heat treatments were carried out in air in a box furnace at constant temperature within ± 2 °C and were quenched in water at room temperature. Tensile tests were performed at a constant displacement rate corresponding to an initial true strain rate of 0.001 s^{-1}, using a universal testing apparatus, as described previously [12].

2.2 Transmission Electron Microscopy (TEM)

Diffraction contrast imaging by bright field transmission electron microscopy (BF-TEM) and Z-contrast imaging by high angle annular dark field scanning transmission electron microscopy (HAADF-STEM). as well as weak beam dark field (WBDF) imaging were performed using the FEI Titan 80-300, on a T6 specimen which was deformed ~ 4% in tension along TD. The details of TEM specimen preparation by electropolishing were described previously [12]. Notably to obtain quantitative precipitate statistics (i.e. size distribution and volume fraction) the foil thickness was measured using the electron energy-loss spectroscopy (EELS) technique [13,14].

3 MODELING APPROACH

The elastoplastic self-consistent EPSC code [15] was used to simulate the mechanical responses of the T5 and T6 material. The model details have been described previously [15–17]. Notably the twinning-detwinning (TDT) model by Wang et al., [18,19] has been used to model extension twinning. The polycrystal is represented as a collection of crystal orientations with volume fractions chosen to reproduce the experimentally measured initial texture [12], which was found to be weaker in the T6 condition, as compared to T5. To simulate uniaxial tension along TD and ND, straining increments of 2×10^{-5} were imposed parallel to one direction while the normal stresses along the other two perpendicular directions and all shear stresses were set to zero. Note that no fitting was performed for the T6, precipitation strengthened case.

4 RESULTS

4.1 Precipitate microstructure

The precipitates in the Mg alloy, WE43, occur in two morphologies [7,8,16,17]: i) approximately equiaxed (globular) in shape and ii) plate shaped on the $\{1\bar{2}10\}$ planes. The habit plane and crystallographic orientation relationship of the plate shaped precipitates is shown schematically in Fig. 1. Notably, there are 3 variants of the plate-shaped precipitates and they form a triangular array on the basal plane when observed along the c-axis of the Mg matrix [6,7]. TEM micrographs of the initial microstructures collected with zone axes [0001] and $\langle 10\bar{1}0\rangle$ were used to fully characterize the length, width and thickness of the precipitates, as documented in a previous publication [12], and the results are summarized in Table 1.

Table 1: Precipitate dimensions and volume fraction for WE43 after T5 and T6 heat treatment. Note that the data come from reference [12]**.**

	Length	Width	Thickness	Vol. fraction (%)
T5 plates	22.67 ± 9.3	10.92 ± 2.9	1.77 ± 0.5	1.57
T5 globules	7.52 ± 1.8			0.98
T6 plates	37.23 ± 11.8	16.83 ± 5.2	2.61 ± 1.3	1.92
T6 globules	9.44 ± 2.3			0.76

A dark field (DF) composite micrograph (Fig. 2a), obtained with the electron beam parallel to $\langle 10\bar{1}0\rangle_{\mathrm{Mg}}$, shows a large area of the Mg matrix containing precipitates. From this micrograph, which was taken on a specimen deformed 4% in tension, it is evident that there is a band within which the plates are severely bent due to consecutive shearing by many gliding dislocations. The band is parallel to the basal plane of the matrix, representing localized basal dislocation slip. Higher magnification micrographs (Fig. 2b and c) reveal that the precipitates are sheared by the basal dislocations. Viewing from the $\langle 10\bar{1}0\rangle$ direction, the three variants of $\{11\bar{2}0\}$ plate precipitates appear either edge-on or at inclined orientations, exhibiting the narrow thickness plane or the broad inclined face of the plate respectively. For the edge-on plate in the upper-right corner of Figure 2(c), two interface steps can be seen, produced by basal dislocation shearing. The widths of the two large steps labeled 3 and 4 are measured to be 3.8 nm and 2.9 nm. The combined displacement corresponds to the passage of 21 dislocations ($b = 0.32$ nm). Using the sheared distance and the distance between the next sheared planes (96.3 nm between planes 2 and 5 in Figure 2(c)), the local shear strain γ is calculated to be 7.1%, which is approximately equal to a normal strain ε of $\gamma/\sqrt{3} = 4.1\%$, which compares well to the macroscopic tensile strain of 4%.

The orientation relationship between the $\{11\bar{2}0\}$ β' precipitates and the matrix is known as $(100)_{\beta'}//(1\bar{2}10)_{\mathrm{Mg}}$ and $[001]_{\beta'}//[0001]_{\mathrm{Mg}}$, and the lattice parameters of the base centered orthorhombic β' phase are $a_{\beta'} = 2\,a_{Mg}$, $b_{\beta'} = 4\sqrt{3}\,a_{Mg}$ and $c_{\beta'} = c_{Mg}$ [6,9,11,20,21]. For this reason, it is revealing to examine bright field (BF) micrographs (Fig. 3) obtained near the [0001] zone axis using diffraction vectors $\boldsymbol{g} = (1\bar{1}00)$, $(10\bar{1}0)$ and $(0\bar{1}10)$. The $\boldsymbol{g}\cdot\boldsymbol{b} = 0$ invisibility criterion reveals that the precipitates have been sheared by all three types of basal dislocations with a_1, a_2 and a_3 Burgers vectors, but always by the one with the Burgers vector perpendicular to the broad face of the precipitate plate. Note that certain lines of contrast become invisible within each of the three micrographs. The pattern of contrast visibility/invisibility corresponds to precipitate shearing by dislocations with the crystallographically admissible $\langle a\rangle$ Burgers vector from the matrix which is parallel to the $a_{\beta'}$ direction within the precipitate $\left(\langle a\rangle_{Mg}||a_{\beta'}\right)$. Note that a complete lattice translation in the β' crystal necessitates two $\langle a\rangle_{Mg}$ dislocations, whereas the passage of one $\langle a\rangle_{Mg}$ vector in the β' phase creates an anti-phase boundary (APB).

4.2 Modeling the strength of Mg alloy WE43 in the T5 temper

In a previous study [11], a set of initial yield and strain hardening parameters were developed to describe the constitutive response T5 material using elastoplastic self-consistent (EPSC) modeling (the so-called inverse modeling approach). In addition, the relative contribution of the different strengthening mechanisms on the CRSS values of the different deformation modes were also obtained based on theoretical calculations. The total contribution of precipitates, to the strength of basal slip, was previously found to be 55 MPa according to the inverse polycrystal modeling approach and assuming Raeisinia et al.'s Hall-Petch coefficient [22].

The precipitate size and volume fraction is reported in Table 1. Using these data, Orowan bowing calculations (Table 2) for non-shearable precipitates (after correcting for non-random distribution according to the simulations of Foreman and Makin [23] and for an error in the previous estimates of the precipitate number density[1]), suggests the strength contribution from globules to be 48 MPa and 85 MPa for the plates, which leads to a total precipitate contribution of 98 MPa, using the Pythagorean superposition principle [24]. The predicted Orowan strengthening of the basal slip system ($\Delta\tau$ total) of 98 MPa is a significant overestimate of the measured strength increment of 55 MPa. However, the Orowan calculations for strength contributions on the prismatic <a> and <c+a> slip systems are within 10% of the EPSC values (Table 2). Based on this analysis, and in addition to the TEM observations, it is concluded that the precipitates are sheared by basal <a> dislocations, but not the non-basal <a> and <c+a> dislocations. Orowan strength predictions are therefore an appropriate treatment for non-basal <a> and <c+a> dislocations, but the observed shearing basal <a> dislocations necessitates a new strengthening model.

Table 2: Summary of Orowan strengthening estimates based on size and volume fraction reported in Table 1 for T5 and T6 material.

T5				**T6**			
	$\Delta\tau$ plate	**$\Delta\tau$ globule**	**$\Delta\tau$ total**		**$\Delta\tau$ plate**	**$\Delta\tau$ globule**	**$\Delta\tau$ total**
Basal	85	48	98	Basal	74	36	82
prismatic	58	48	75	prismatic	48	36	60
c+a	121	71	140	c+a	108	54	120

[1] Previous estimates [11] of the TEM sample thickness, which are required to estimate the precipitate volume fraction and number density, used the Convergent Beam Electron Diffraction (CBED) method and were found to be in error. Current estimates employ the ratio of the first plasmon peak intensity to the zero loss peak intensity within the Electron Energy Loss Spectrum (EELS).

Table 3: Voce hardening parameters for T5 temper obtained from Bhattacharyya et al., [11] **and the precipitate contributions for each mode.**

	τ_0	τ_1	θ_0	***Precipitate contribution for T5*** $(\tau_{EPSC} - \tau_{HP[34]} - \tau_{solute} - \tau_{single\ xtal} - \tau_{forest})$
Basal	68	40	170	55
Prismatic	145	90	170	68
<c+a> 2nd order	210	205	350	133
Tensile twin	130	0	150	-

5 DISCUSSION

When individual dislocations sample an array of precipitates, force equilibrium dictates that the resisting force offered by the particle, *F*, is balanced by the line tension of the dislocation:

$$F = 2T sin\theta_c \tag{1}$$

where θ_c is the critical angle to which dislocations are forced to bow out. The general form of the expression describing such obstacle strengthening is given by [25–27]:

$$\tau_{shear} = \left(\frac{F}{2T}\right)^{\frac{3}{2}} \left(\frac{2T}{bl_{ppt}}\right) \tag{2}$$

Note that the strength of the obstacle, *F*, is expressed relative to the dislocation line tension, *T*. In the limit when $\theta_c = 90°$ the strength of the obstacle $F = 2T$, and we recover the familiar Orowan bowing expression. If we treat the plate and globular precipitates collectively, with an average effective radius of 2.8 nm and inter-particle spacing of 25 nm (based upon the data in Table 1), the critical angle for basal shearing of the precipitates is shown to be 24°. In addition to the direct evidence provided by TEM, this approximate analysis shows that the particles in Mg

alloy, WE43, are weak obstacles, offering a shear resistance which is higher than the c-axis rods observed in Mg-Zn [5] but lower than that observed in Al-Zn-Cu-Mg [28].

For the case of particle shearing, a number of possible mechanisms can be operative/controlling. These include stacking fault energy mismatch (most relevant to the case of disordered precipitates with the same crystal structure as the matrix), interface creation, modulus mismatch, coherency strain, and anti-phase domain boundary (APB) order strengthening [25–27,29]

It is generally accepted that the mechanism of interface creation contributes a relatively small amount to the strength (e.g. [25,27]), and given the fact that the interfacial energies for these coherent precipitates are small [30], this will not be considered further. *Ab initio* density functional theory calculations of the elastic properties of Mg-RE intermetallic compounds show most of the components of the single crystal stiffness tensors to be similar to those of Mg [31], so the strengthening effect of modulus mismatch is also assumed here to be small.

There is no doubt that there are coherency strains associated with the precipitates in the present alloys [30,32], which strongly influence precipitate shape and transformation kinetics. Presently, there is no analytical expression describing how such complex strain fields interact with dislocations. However, the presence of such coherency strain fields will affect dislocation motion, whether they ultimately shear or bow around the precipitates. The fact that the Orowan bowing expression well-describes the strengthening behavior of non-basal <a> and <c+a> dislocations suggests that coherency strengthening effects are modest.

Finally, the requirement that perfect dislocations have Burgers vectors which connect crystal lattice points leaves no doubt that perfect <a> dislocations from the matrix will become super-partial dislocations within the precipitate which will create APBs in their wake. For this

reason, we hypothesize that APB strengthening is the major contributor to the resistance to shearing. The subsequent analysis will show this hypothesis to be reasonable (i.e., a reasonable APB energy emerges). However, accounting for coherency strains is viewed as fertile ground for future study and, if found significant, would lead to the conclusion that the APB is lower than that obtained here.

5.1 Strengthening due to shearable precipitates

The TEM results presented in Section 4.2 show clear evidence of shearing of the plate precipitates by basal dislocations. As discussed in the previous section, the following model assumes that antiphase domain boundary (APB) or order strengthening is the dominant strengthening mechanism. In this scenario, as the first (leading) dislocation shears precipitates by sampling them at a spacing l_1, it creates an antiphase domain boundary within the precipitate, which attracts another (trailing) dislocation to restore the order. The leading and trailing dislocations are also subjected to Peach-Kohler forces due to the applied stress, τ, and mutual repulsion. The classic analysis of a pair of dislocations interacting with shearable precipitates (originally developed to describe Ni-based superalloys [33,34]) employs this force equilibrium:

$$\tau b l_1 + \frac{\mu b^2}{2\pi(1-\nu)\Lambda} l_1 - \gamma_{APB} d_1 = 0 \tag{3}$$

$$\tau b l_2 - \frac{\mu b^2}{2\pi(1-\nu)\Lambda} l_2 + \gamma_{APB} d_2 = 0 \tag{4}$$

where, l_1 and l_2 are the lengths of the leading and trailing dislocations involved in the cutting process, respectively, and d_1 and d_2 are the corresponding lengths of the segments of the dislocations that are cutting the precipitates. Up to the peak-aged condition, it is assumed that the pair of dislocations does not lie within the same precipitate; i.e., it is the case of weak coupling. Only when the precipitates coarsen to significantly large sizes, as generally is the case in over-

aged condition, both dislocations can lie inside the same precipitates [35–37]. This latter case of strong coupling is considered in some detail in the Supplementary material.

Dividing Eqs. 3 and 4 by l_1 and l_2, respectively, and adding them together gives the shear resistance due to the cutting process as:

$$\tau = \frac{\gamma_{APB}}{2b}\left(\frac{d_1}{l_1} - \frac{d_2}{l_2}\right) \tag{5}$$

Similarly, the relationship between the dislocation spacing and the APB energy can be established by subtracting Eq. 4 from Eq. 3:

$$\Lambda = \frac{\mu b^2}{2\pi(1-\nu)\gamma_{APB}\left(\frac{d_1}{l_1}+\frac{d_2}{l_2}\right)} \tag{6}$$

In order to proceed further, we have to make assumptions about the various lengths d_i and l_i. The sampling length l_i depends on how strongly the dislocation is bowed around the precipitates. When the precipitates are small, the shear resistance offered by them is low and thus the dislocations can overcome them at low stress levels by remaining relatively straight. In these circumstances, the average distance between the particles contacted by the dislocation line is larger than the inter-particle spacing. As the precipitate size increases, a higher stress is required to overcome them and as a result the dislocations bow out strongly, thereby sampling a larger number of obstacles. This reduction in sampling distance continues until it reaches a lower bound, which is the inter-particle spacing, λ. The sampling distance cannot increase indefinitely, rather a theoretical upper bound exists which holds true for a perfectly straight dislocation and is given by the spacing of random particles along a straight line, l_{max}. The commonly employed Friedel sampling length, l_F, lies in between these two limits.

For the leading dislocations, it is assumed that the most relevant sampling length is λ. As far as the trailing dislocations are concerned, TEM observations on Ni based superalloys have shown they remain straight at least until the peak-aged condition, due to repulsion from the

leading dislocation. Thus the appropriate sampling distance for them is l_{max}. The d_i for both dislocations is assumed to be the average diameter of the precipitates on the slip plane. Without additional information, it is assumed that the same configuration is applicable for this Mg alloy as well, and the results of this analysis will prove to be consistent with these assumptions.

The case of spherical precipitates of radius r_0^{sphere}, mean planar area a_p^{sphere} and area number density n_s^{sphere} is described earlier [26,29,35,37–39] and leads to the following shear resistance, based upon Eq. 5:

$$\tau_{sphere} = \frac{\gamma_{APB}}{2b}\left(\frac{2r_p^{sphere}}{\lambda_{basal}^{sphere}} - f\right) \tag{7}$$

For a triangular array of plate shaped precipitates, the effective interparticle spacing for basal slip is given by [1]:

$$\lambda_{basal}^{plate} = \frac{1.075\sqrt{wt}}{\sqrt{f}} - 0.5w - 0.866t \tag{8}$$

where w, t and f are the width, thickness and volume fraction of the precipitates, respectively. The intersection of the plates with the basal plane can be approximated as an ellipse and thus the mean planar area of these plates on the basal plane, a_p^{plate} is equal to $\frac{\pi wt}{4}$. Thus, an equivalent diameter on the slip plane for these precipitates can be defined as:

$$D_p^{plate} = \sqrt{\frac{4a_p^{plate}}{\pi}} = \sqrt{wt} \tag{9}$$

The maximum possible sampling distance, l_{max}^{plates} can be obtained in a similar manner as the spheres:

$$l_{max}^{plates} = \frac{a_p^{plates}}{fD_p^{plates}} = \frac{\frac{\pi wt}{4}}{f\sqrt{wt}} = \frac{\pi}{4f}\sqrt{wt} \tag{10}$$

The ratio d_2/l_2 then becomes:

$$\frac{d_2}{l_2} = \frac{D_p^{plate}}{l_{max}^{plate}} = \frac{\sqrt{wt}}{\frac{\pi}{4f}\sqrt{wt}} = \frac{4}{\pi} f = 1.27f \cong f \tag{11}$$

which is not very dissimilar to that of spheres [37]. In the end, the shear resistance can be obtained from Eq. 5 as:

$$\tau_{plate} = \frac{\gamma_{APB}}{2b}\left(\frac{D_p^{plate}}{\lambda_{basal}^{plate}} - f\right) = \frac{\gamma_{APB}}{2b}\left(\frac{\sqrt{wt}}{\frac{1.075\sqrt{wt}}{\sqrt{f}} - 0.5w - 0.866t} - f\right) \tag{12}$$

For alloys which contain both plate and globular precipitates, like Mg alloy WE43, the total shear resistance due to precipitates can thus be obtained using a Pythagorean superposition of the individual contributions (i.e. Eq. 7 for spheres and Eq. 12 for plates). Given the lack of TEM evidence to the contrary, it is assumed that non-basal dislocations loop around the precipitates, rather than shear through them.

In order to proceed further, an estimate of the APB energy for basal dislocation shearing of the β' phase precipitates is required. Without any experimental data or values determined by first principles calculations, one strategy to obtain the APB energy is to treat it as a fitting parameter and estimate its value by equating the formulation presented in Section 5.1 to the total precipitate strength contribution of 55 MPa for basal slip

$$\tau_{ppt}^{T5} = \sqrt{\tau_{globules}^2 + \tau_{plates}^2} = \sqrt{36^2 + 42^2} = 55 \text{ MPa} \tag{13}$$

This methodology leads to an APB energy of 210 mJ/m^2, and with this estimate of the APB energy, the flow behavior of the T6 material can be predicted.

5.2 Predicting the flow strength of Mg alloy WE43 in the T6 temper

In order to predict the response of the material in the T6 temper, several assumptions were required. First, although there is a significant difference in the yield stress between T5 and T6, the hardening behavior at higher strain levels is quite similar. Thus, in order to minimize the

number of free parameters, the Voce hardening parameters, τ_1 and θ_0 for each mode, were assumed to be the same as that for T5.

The solid solution strengthening for basal slip is calculated from Yasi et al. [40], assuming the same solute content in the matrix as that for T5, since the volume fraction of the precipitates are quite similar for both cases (~2.5%) . For prismatic slip the solute strengthening is assumed to be ~0 [11] and for <c+a> slip it is essentially unknown.

The precipitation strengthening contribution for basal slip is computed following the same strategy as that for T5 and using an APB energy of 210 mJ/m^2. This leads to a total contribution due to precipitate strengthening of 57 MPa according to:

$$\tau_{ppt}^{T6} = \sqrt{\tau_{globules}^2 + \tau_{plates}^2} = \sqrt{32^2 + 47^2} = 57 \text{ MPa} \quad (14)$$

The resulting strength contribution is only 4% larger than that of T5, which is not surprising, given the fact that the size and the volume fraction of the strengthening precipitates is only slightly larger for this temper. For prismatic and <c+a> slip, the Orowan strengthening values shown in Table 2 are used.

There is no established model for the effect of precipitates, either shearable or non-shearable, on the strength of twinning [2,3]. For grain size strengthening, the Hall-Petch coefficients of Raeisinia et al., [22] is used in order to be consistent with the earlier study. Given such sparse information, the fitted EPSC model τ_0 for T5 (130 MPa) was only adjusted for grain size and used for the T6 case. Since the H-P coefficient of twinning was not obtained by Raeisinia et al. [22], Wang and Choo's value [41] was used to correct for the grain size difference (Table 4). Table 5 shows the initial CRSS, τ_0, calculated by taking into account the abovementioned strengthening contributions according to:

$$\tau_{CRSS}^{T6} = \tau_0 + \tau_{gb} + \tau_{ss} + \tau_{ppt} \quad (15)$$

Table 4: The effect of grain size on individual deformation modes for T5 and T6 material, obtained using Hall Petch coefficients from Raeisinia et al. [22]**. *Only for twinning, Wang and Choo** [41] **value is used.**

Deformation mode	Hall Petch coefficient k (MPa-mm$^{1/2}$)	$\Delta\tau_{HP}$ T5 (MPa)	$\Delta\tau_{HP}$ T6 (MPa)
Basal	0.42	3	1
Prismatic	3.72	28	13
Pyramidal <c+a>	4.71	35	16
Extension twinning*	3.48	26	12

Table 5: The strengthening contribution from lattice resistance, τ_0, grain boundaries, τ_{gb}, solid solution, τ_{ss} and precipitates, τ_{ppt} on individual slip modes for T6 temper. For the twinning mode the T5 CRSS (130 MPa) is only modified in order to take into account the grain size difference. The θ_0 and τ_1 are the same as that of the T5 temper [11]**.**

Deformation mode	τ_0	τ_{gb}	τ_{ss}	τ_{ppt}	$\boldsymbol{\tau_{CRSS}^{T6}}$	θ_0	τ_1
Basal	0.5	1	8	56	**66**	170	40
Prismatic	48	13	0	60	**121**	170	90
Pyramidal <c+a> 2nd order	40	16	-	120	**176**	350	205
Extension twinning*	8	12	-	-	**116**	150	0

The simulated curves for the TD (Fig. 4a) show good overall agreement (within 2% at ε = 0.02) with the experimentally observed flow behavior subsequent to aging. The simulated results confirm that the T6 heat treatment did not alter the hardening behavior significantly. Regarding the ND case (Fig. 4b), the simulated flow curves over-predict flow stress by 10 %, which is not surprising given that a similar level of overestimation was observed for the training data set (the T5 case) [11].

It is worth mentioning that precipitates of up to 4 nm can be sheared in an Al-Zn-Cu-Mg alloy, (e.g. [28]). Similarly, earlier work on Mg-5% Zn by Wang et al., [5] showed that rod-shaped precipitates of 10 nm radius were sheared by basal <a> dislocations. Given these observations and the current precipitate sizes, it is not surprising that they are also sheared by basal slip.

A final point worth discussing is the fact that the critical size may not involve a transition to bowing but one of 'strong coupling' where the leading and the trailing dislocations may interact within the same precipitate. Such 'strong-coupling' scenarios were first analyzed by Huther and Reppich [36], and Argon [27] subsequently modified the analysis by taking into account the additional interaction of the two dislocations in such configuration. Both analyses show that the maximum shear resistance offered by the precipitate is attained when the trailing dislocation just enters the precipitate. The shear resistance in the strong-coupling regime shows a relatively weak (inverse square root) dependence on the precipitate size, instead of the stronger inverse dependence of Orowan bowing. With a further increase in particle size, a subsequent transition to Orowan bowing may be observed. In order to explore the possibilities, a parametric study has been carried out (Fig. 5) which shows the shear resistance as a function of the precipitate size for APB energies of 100 and 400 mJ/m^2, for a precipitate volume fraction of 5%.

Firstly, the plots show that the shear resistance increases with increase in APB energy, as expected. Perhaps it is more interesting to observe that for a low APB energy, the peak resistance is associated with a transition from weak coupling to strong coupling (at <D> ~ 40 nm) rather than to Orowan bowing. In these circumstances, the precipitates are still sheared by the dislocations, however, their shear resistance decreases as they coarsen. As the APB energy increases, the spacing between the two partial dislocations decreases and repulsive stress

increases to such an extent that it becomes energetically favorable to bow around the precipitates instead of shearing them (at <D> ~70 nm for the example shown here). For the case of higher APB energy, Orowan bowing offers less resistance than the strong-coupling case, for spherical particles of all sizes. A similar analysis of the strong-pair coupling case for elliptical precipitates is derived and discussed in the Supplementary material.

WE43 is one of the strongest commerical Mg alloys, and the current TEM investigation in conjuction with strength modeling have revealed that the strengthening precipitates are sheared by basal slip. This work has significant implications for Mg alloy design strategies by emphasizing the importance of accounting for the effect of precipitate (or GP zone) shearing on the strength of Mg alloys. In particular, it emphasizes the need for accurate estimates of APB energies (γ-surfaces), of the candidate strengthening phases. Finally, the present study also highlights the age-old problem in precipitation hardenable Mg alloys [42]: the strength of Mg alloys is most strongly limited by the low number densities and volume fractions of these strengthening phases.

6 CONCLUSIONS:

Transmission electron microscopy (TEM) shows that the prismatic plate-shaped precipitates in Mg alloy, WE43, are shearable by basal slip of <a> dislocations. The known orientation relationship between the ordered, orthorhombic phase and the hexagonal close-packed Mg matrix phase is such that two <a> dislocations from the matrix would be required to restore the order in the β' phase. Thus, it appears that the mechanism by which these precipitates strengthen the basal slip mechanism in WE-series alloys is order (or anti-phase domain boundary, APB) strengthening.

A model for basal slip strengthening from shearable precipitates is introduced, based upon prior work validated for Ni-based superalloys. Using this model, the APB energy is estimated to be 210 mJ/m^2. The modelling has shown that for this alloy, the peak-aging condition may be defined by a transition from weak- to strong-coupling between the leading and trailing dislocations, rather than a transition from shearing to bowing.

Precipitate strengthening predictions based on the classical Orowan looping model for prismatic and pyramidal <c+a> dislocations agree well with the values obtained using crystal plasticity modeling. Since no evidence of shearing from these non-basal dislocations was observed using TEM, it has been concluded that prismatic <a> and pyramidal <c+a> dislocations are unable to shear the precipitates, and instead bow around them during plastic deformation. This is suggested to be due to both the shape and crystallography of the particles.

Using the TEM characterization of the particles, and the newly developed particle shearing model, EPSC was used to validate the accuracy of our strength model on WE43 in the T6 condition. The tensile flow curves for T6 were predicted with 2% and 10% accuracy along the transverse and normal directions, respectively.

The results of this study emphasize the fact that alloy and heat treatment process designers will require knowledge of the relative shearability of candidate precipitates and GP zones. In order to make accurate strengthening predictions, information such as the APB energies and coherency strains of candidate strengthening phases may be required. Most importantly, in the present magnesium alloy, Orowan bowing strongly over-predicts the strengthing of the basal slip system, and assuming simplistic Orowan bowing will not provide realistic strength estimates.

Acknowledgements: The research at U.Va. was sponsored by the United States Army Research Office under contract number W911NF-12-1-0455 monitored by Drs. Suveen Mathaudhu and

David Stepp. The views and conclusions contained in this document are those of the authors and should not be interpreted as representing the official policies, either expressed or implied, of the Army Research Laboratory or the U.S. Government. The U.S. government is authorized to reproduce and distribute reprints for government purposes notwithstanding any copyright notation hereon.

REFERENCES

[1] J.F. Nie, Effects of precipitate shape and orientation on dispersion strengthening in magnesium alloys, Scr. Mater. 48 (2003) 1009–1015. doi:10.1016/S1359-6462(02)00497-9.

[2] J.D. Robson, N. Stanford, M.R. Barnett, Effect of precipitate shape on slip and twinning in magnesium alloys, Acta Mater. 59 (2011) 1945–1956. doi:10.1016/j.actamat.2010.11.060.

[3] J.D. Robson, N. Stanford, M.R. Barnett, Effect of Precipitate Shape and Habit on Mechanical Asymmetry in Magnesium Alloys, Metall. Mater. Trans. A. 44 (2012) 2984–2995. doi:10.1007/s11661-012-1466-0.

[4] F. Wang, J.J. Bhattacharyya, S.R. Agnew, Effect of precipitate shape and orientation on Orowan strengthening of non-basal slip modes in hexagonal crystals, application to magnesium alloys, Mater. Sci. Eng. A. 666 (2016) 114–122. doi:10.1016/j.msea.2016.04.056.

[5] J. Wang, N. Stanford, Investigation of precipitate hardening of slip and twinning in Mg5%Zn by micropillar compression, Acta Mater. 100 (2015) 53–63. doi:10.1016/j.actamat.2015.08.012.

[6] J.F. Nie, B.C. Muddle, Characterisation of strengthening precipitate phases in a Mg–Y–Nd alloy, Acta Mater. 48 (2000) 1691–1703. doi:10.1016/S1359-6454(00)00013-6.

[7] J.F. Nie, X.L. Xiao, C.P. Luo, B.C. Muddle, Characterisation of precipitate phases in magnesium alloys using electron microdiffraction, Micron. 32 (2001) 857–863. doi:10.1016/S0968-4328(00)00094-9.

[8] C. Antion, P. Donnadieu, F. Perrard, A. Deschamps, C. Tassin, A. Pisch, Hardening precipitation in a Mg-4Y-3RE alloy, Acta Mater. 51 (2003) 5335–5348. doi:10.1016/S1359-6454(03)00391-4.

[9] E. Sitzmann, E.A. Marquis, Chemistry and morphology of β′ precipitates in an aged Mg-Nd-Y-Zr alloy., Philos. Mag. Lett. 95 (2015) 7–13.

[10] S.R. Agnew, R.P. Mulay, F.J. Polesak, C.A. Calhoun, J.J. Bhattacharyya, B. Clausen, In situ neutron diffraction and polycrystal plasticity modeling of a Mg–Y–Nd–Zr alloy: Effects of precipitation on individual deformation mechanisms, Acta Mater. 61 (2013)

3769–3780. doi:10.1016/j.actamat.2013.03.010.
[11] J.J. Bhattacharyya, F. Wang, P.D. Wu, W.R. Whittington, H. El Kadiri, S.R. Agnew, Demonstration of alloying, thermal activation, and latent hardening effects on quasi-static and dynamic polycrystal plasticity of Mg alloy, WE43-T5, plate, Int. J. Plast. 81 (2016) 123–151. doi:10.1016/j.ijplas.2016.01.005.
[12] J.J. Bhattacharyya;, F. Wang;, P. McQuade, S.R. Agnew, Deformation and fracture behavior of Mg alloy, WE43, after various aging heat treatments, Mater. Sci. Eng. A. (2017).
[13] T. Malis, S.. Cheng, R.. Egerton, Log-Ratio Technique for Specimen-Thickness Measurement in the TEM, J. Electron Microsc. Techinique. 8 (1988) 193–200. papers3://publication/uuid/5C3A4951-E317-4E4A-B34E-C626F89F4428%5Cnpapers3://publication/uuid/1E7DE96E-137D-4E8E-A975-D0B827ADDC55.
[14] R.F. Egerton, Electron energy loss in the electron microscope, Plenum, New York. 160 (1996) 165–169.
[15] P.A. Turner, C.N. Tomé, A study of residual stresses in Zircaloy-2 with rod texture, Acta Metall. Mater. 42 (1994) 4143–4153. doi:10.1016/0956-7151(94)90191-0.
[16] B. Clausen, C.N. Tomé, D.W. Brown, S.R. Agnew, Reorientation and stress relaxation due to twinning: Modeling and experimental characterization for Mg, Acta Mater. 56 (2008) 2456–2468. doi:10.1016/j.actamat.2008.01.057.
[17] C.J. Neil, J.A. Wollmershauser, B. Clausen, C.N. Tomé, S.R. Agnew, Modeling lattice strain evolution at finite strains and experimental verification for copper and stainless steel using in situ neutron diffraction, Int. J. Plast. 26 (2010) 1772–1791. doi:10.1016/j.ijplas.2010.03.005.
[18] H. Wang, P.D. Wu, C.N. Tomé, J. Wang, A constitutive model of twinning and detwinning for hexagonal close packed polycrystals, Mater. Sci. Eng. A. 555 (2012) 93–98. doi:10.1016/j.msea.2012.06.038.
[19] H. Wang, P.D. Wu, J. Wang, C.N. Tomé, A crystal plasticity model for hexagonal close packed (HCP) crystals including twinning and de-twinning mechanisms, Int. J. Plast. 49 (2013) 36–52. doi:10.1016/j.ijplas.2013.02.016.
[20] K. Saito, K. Hiraga, The Structures of Precipitates in an Mg-0.5 at%Nd Age-Hardened Alloy Studied by HAADF-STEM Technique, Mater. Trans. 52 (2011) 1860–1867. doi:10.2320/matertrans.M2011163.
[21] M. Nishijima, K. Yubuta, K. Hiraga, Characterization of β′ Precipitate Phase in Mg-2 at%Y Alloy Aged to Peak Hardness Condition by High-Angle Annular Detector Dark-Field Scanning Transmission Electron Microscopy (HAADF-STEM), Mater. Trans. 48 (2007) 84–87. doi:10.2320/matertrans.48.84.
[22] B. Raeisinia, S.R. Agnew, A. Akhtar, Incorporation of Solid Solution Alloying Effects into Polycrystal Modeling of Mg Alloys, Metall. Mater. Trans. A. 42 (2010) 1418–1430. doi:10.1007/s11661-010-0527-5.
[23] A.J.E. Foreman, M.J. Makin, Dislocation movement through random arrays of obstacles, Philos. Mag. 14 (1966) 911–924.
[24] T.J. Koppenaal, D. Kuhlmann-Wilsdorf, The effect of prestressing on the strength of neutron-irradiated copper single crystals, Appl. Phys. Lett. 4 (1964).
[25] V. Gerold, Precipitation hardening, Dislocations in Solids. 4 (1980) 219–260.
[26] A.. Ardell, Precipitation Hardening, Metall. Trans. A. 16 (1985) 2131–2165.

[27] A.S. Argon, Strengthening mechanisms in crystal plasticity, Oxford: Oxford University Press., 2008.
[28] A. Deschamps, Y. Brechet, Influence of predeformation and ageing of an Al–Zn–Mg alloy—II. Modeling of precipitation kinetics and yield stress, Acta Mater. 47 (1998) 293–305. doi:10.1016/S1359-6454(98)00296-1.
[29] B. Reppich, Particle strengthening, in: H. Mughrabi, R.W. Cahn, P. Hassen, E.J. Kramer (Eds.), Mater. Sci. Technol. - A Compr. Treat., Wiley Online Library, 1993: p. 113.
[30] H. Liu, Y. Gao, J.Z. Liu, Y.M. Zhu, Y. Wang, J.F. Nie, A simulation study of the shape of β' precipitates in Mg-Y and Mg-Gd alloys, Acta Mater. 61 (2013) 453–466. doi:10.1016/j.actamat.2012.09.044.
[31] Y.Z. Ji, A. Issa, T.W. Heo, J.E. Saal, C. Wolverton, L.Q. Chen, Predicting β′ precipitate morphology and evolution in Mg-RE alloys using a combination of first-principles calculations and phase-field modeling, Acta Mater. 76 (2014) 259–271. doi:10.1016/j.actamat.2014.05.002.
[32] A.R. Natarajan, A. Van der Ven, A unified description of ordering in HCP Mg-RE alloys, Acta Mater. 124 (2017) 620–632. doi:10.1016/j.actamat.2016.10.057.
[33] H. Gleiter, E. Hornbogen, Theorie der Wechselwirkung von Versetzungen mit koh{ä}renten geordneten Zonen (I), Phys. Status Solidi. 12 (1965) 235–250.
[34] H. Gleiter, E. Hornbogen, Beobachtung der Wechselwirkung von Versetzungen mit koh{ä}renten geordneten Zonen (II), Phys. Status Solidi. 12 (1965) 251–264.
[35] L.M. Brown, R.K. Ham, Strengthening methods in crystals, Appl. Sci. London. 9 (1971) 12.
[36] W. Huther, B. Reppich, Interaction of Dislocations with Coherent, Stree-Free Ordered Particles, Zeitschrift Fur Met. 69 (1978) 628–634.
[37] E. Nembach, G. Neite, Precipitation Hardening of Superalloys By Ordered Gamma Prime-Particles, Prog. Mater. Sci. 29 (1985) 177–319. doi:10.1016/0079-6425(85)90001-5.
[38] D. Raynor, J.M. Silcock, Strengthening mechanisms in γ′ precipitating alloys, Met. Sci. J. 4 (1970) 121–130.
[39] R.C. Reed, The superalloys: fundamentals and applications, Cambridge university press, 2008.
[40] J.A. Yasi, L.G. Hector, D.R. Trinkle, First-principles data for solid-solution strengthening of magnesium: From geometry and chemistry to properties, Acta Mater. 58 (2010) 5704–5713. doi:10.1016/j.actamat.2010.06.045.
[41] Y. Wang, H. Choo, Influence of texture on Hall–Petch relationships in an Mg alloy, Acta Mater. 81 (2014) 83–97. doi:10.1016/j.actamat.2014.08.023.
[42] J.B. Clark, Age hardening in a Mg-9 wt.% Al alloy, Acta Metall. 16 (1968) 141–152.
[43] S.I. Rao, T.A. Parthasarathy, D.M. Dimiduk, P.M. Hazzledine, Discrete dislocation simulations of precipitation hardening in superalloys, Philos. Mag. 84 (2004) 3195–3215.

*Figure(s)

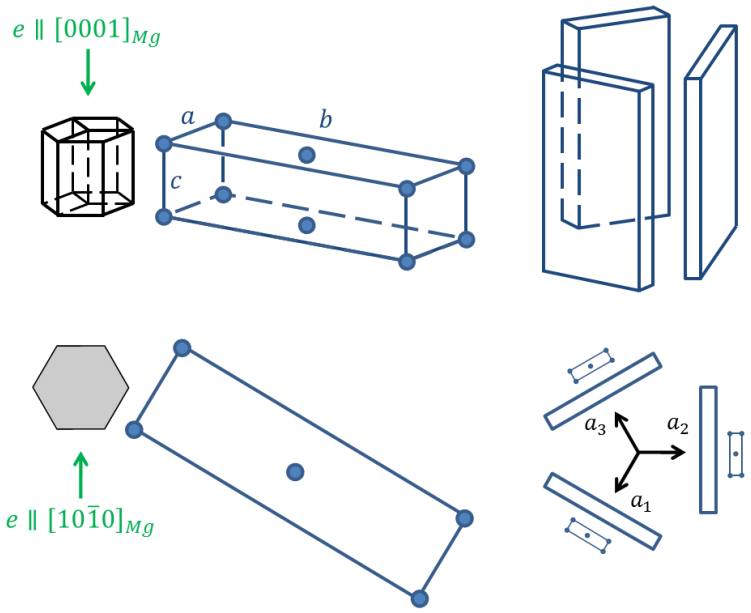

Figure 1: Lattices of Mg (in black) and β' (in blue) precipitates, with the orientation relationship schematically shown on the right.

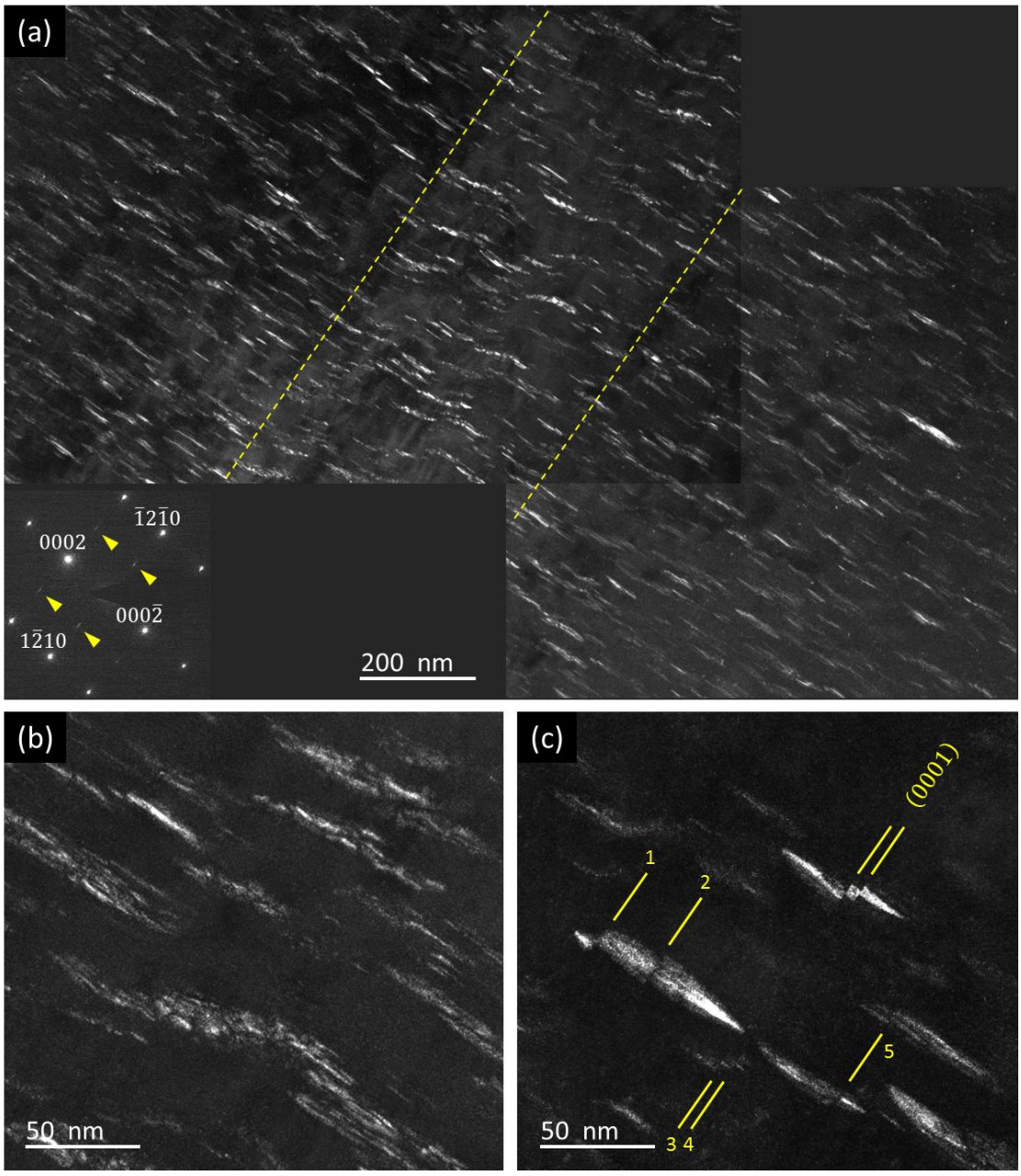

Figure 2: Axial dark field micrographs of sheared β' plate precipitates, obtained using precipitate diffraction spot at $1/2\{1\bar{2}10\}_{Mg}$ in $\langle 10\bar{1}0\rangle_{Mg}$ SAED pattern (the inset in (a)). A band of localized shearing of precipitates by gliding dislocations is delineated in (a) by the dashed lines (b) a region within the deformation band, and (c) presents several discretely sheared plate precipitates.

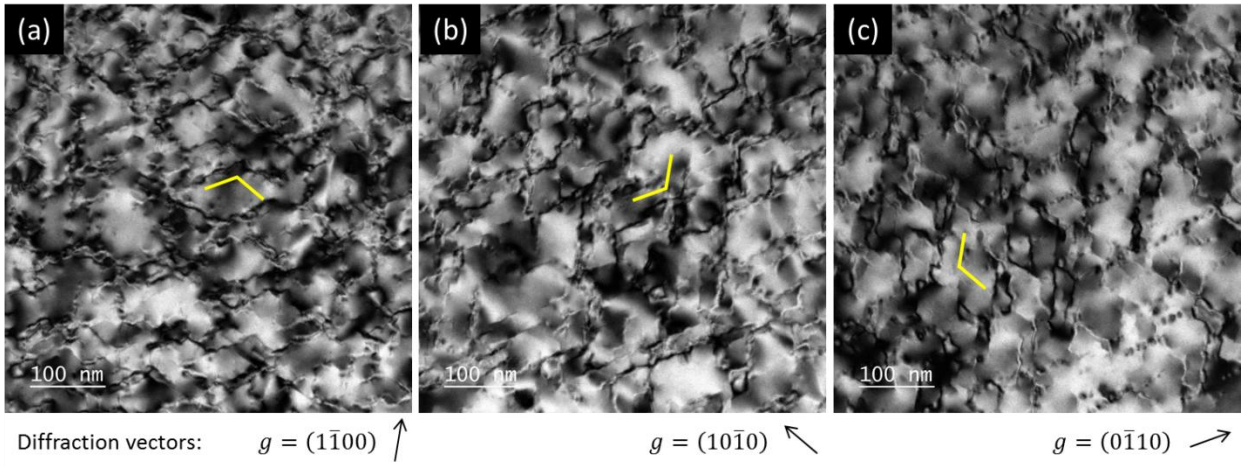

Figure 3: Two-beam BF images of the deformed microstructure obtained near [0001] the zone axis. The diffraction vectors employed are indicated below the micrographs. The lines of visible diffraction contrast are indicated by yellow lines in the respective micrographs.

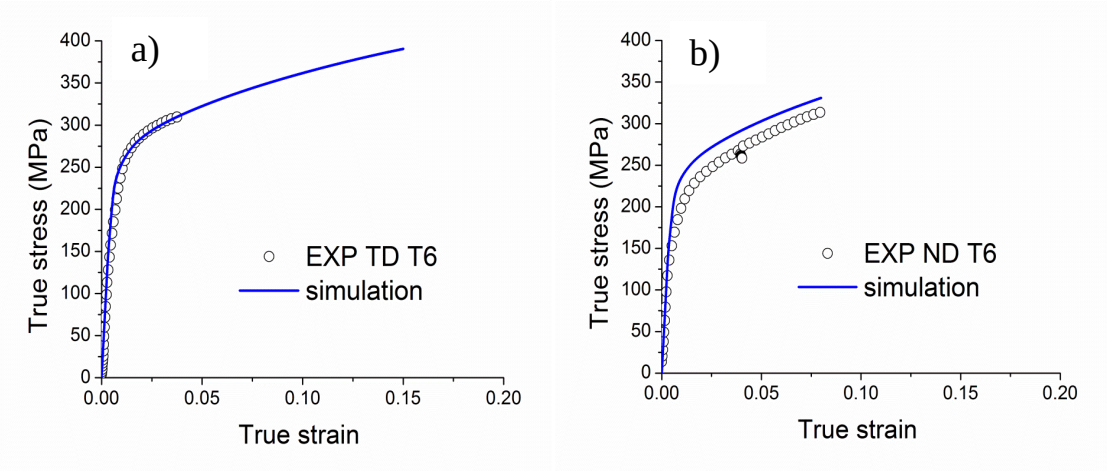

Figure 4: Comparison between measured and simulated tensile flow curves for tests performed on WE43-T6 parallel to the a) transverse (TD) and b) normal (ND) directions, respectively.

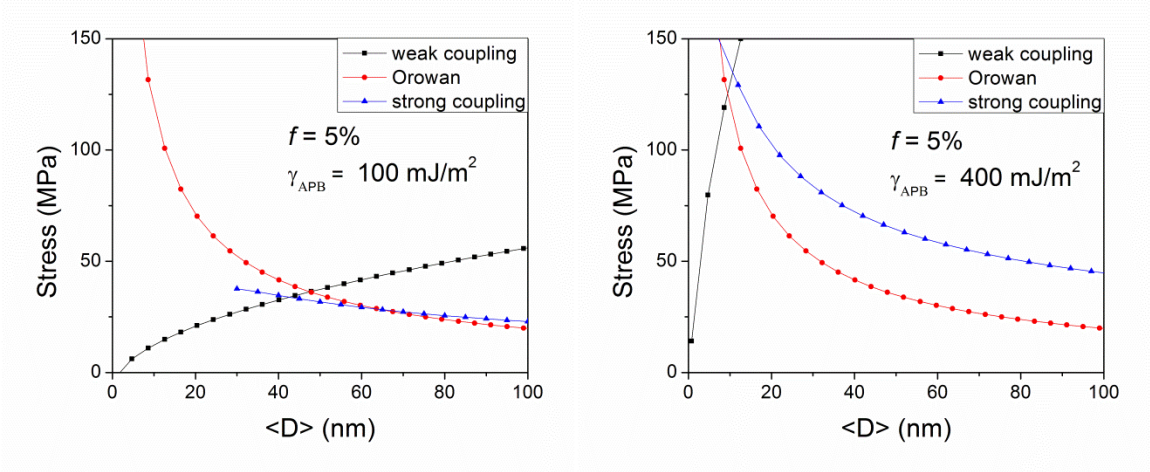

Figure 5: Particle size dependencies of the flow strength due to particle shearing and bowing for a given particle volume fraction (5%), but varying APB energy.

Supplementary Material

Click here to download Supplementary Material: WE43 shearable ppt supplementary material.docx

*Graphical Abstract